Fuel Processing Technology 288 (2026) 108465

Contents lists available at ScienceDirect

Fuel Processing Technology

journal homepage: www.elsevier.com/locate/fuproc

Catalytic deoxygenation waste cooking oil into green diesel range hydrocarbons in a continuous processing over monolayered CoS-MnS supported Al_2S_3 catalyst

Laith K. Obeas [a,d], G. Abdulkareem Alsultan [a,e,i,*], G. Mohamed Alsultan [a,j], N. Asikin-Mijan [b,**], N. Asma-Samsudin [b], Hwei Voon Lee [c], Stella Jovita [e], Didik Prasetyoko [e,**], Maadh Fawzi Nassar [a], Tonni Agustiono Kurniawan [f], Dai-Viet N. Vo [g,h], Yun HinTaufiq-Yap [a,**]

[a] Catalysis Science and Technology Research Centre (PutraCat), Universiti Putra Malaysia, 43400 UPM Serdang, Selangor, Malaysia
[b] Department of Chemical Sciences, Faculty of Science and Technology, Universiti Kebangsaan Malaysia, 43600 UKM Bangi, Selangor Darul Ehsan, Malaysia
[c] Nanotechnology and Catalysis Research Centre (NANOCAT), University of Malaya, Kuala Lumpur 50603, Malaysia
[d] Technical Institute of Babylon, Al-Furat Al-Awsat Technical University (ATU), Iraq
[e] Department of Chemistry, Faculty of Science and Data Analytics, Institut Teknologi Sepuluh Nopember (ITS), Sukolilo, Surabaya 60111, Indonesia
[f] College of the Environment and Ecology, Xiamen University, Xiamen, China
[g] Center for Global Health Research, Department of Environmental Science, Saveetha Medical College, Saveetha Institute of Medical and Technical Sciences, India
[h] Graduate School of Energy and Environment, Korea University, 145 Anam-ro, Seongbuk-gu, Seoul 02841, Republic of Korea
[i] Fuel and Energy Techniques Eng. Department, South Technical University, Al-Zubair Street, Basra, Iraq
[j] Department of Petroleum Project Management College of Industrial Management of Oil and Gas, Basrah University for Oil and Gas, Basra, Iraq

ARTICLE INFO

Keywords:
Green diesel
Heterogeneous catalyst
Deoxygenation
Nano catalyst
Metal oxide

ABSTRACT

The drive towards using carbon neutral fuel sources is based on the need for improved catalytic processes to convert the hydrocarbons in waste derived lipids into quality hydrocarbon products. In this paper, we have developed a CoS-MnS/Al catalyst capable of performing a hydrogen-free deoxygenation process on waste cooking oil (WCO) at exceptionally high productivities, selectivities and stabilities. Structural characterization of the catalyst has been performed through a range of methods including X-ray diffraction (XRD), X-ray photoelectron spectroscopy (XPS), N_2 adsorption/desorption (BET), ammonia temperature-programmed desorption (NH_3-TDP) and electron paramagnetic resonance (EPR). These analyses demonstrated that the catalyst forms a unique bifunctional heterostructure composed of three distinct phases; Co3S4, MnS and an interface phase composed of Al2S3. The optimized acid-base properties of the surface along with electronic strain effects associated with the sulfur edge sites allow modulation of all possible C—O bond activation pathways. Optimization of the composition of Co and Mn created a balance of acidity across the catalyst's surface that directed the reactivity to both cooperative hydrodeoxygenation and decarboxylation-decarbonylation reactions resulting in highly effective conversion of triglycerides and free fatty acids to long chain n-paraffins. Under continuous flow conditions and mild temperatures (approximately 300 °C), the CoS0.5MnS0.5/Al catalyst achieved approximately 89% hydrocarbon yield with approximately 93% selectivity to C_{15}-C_{17} diesel-range n-paraffin molecules while demonstrating structural integrity after several reaction cycles. Kinetics were also examined as they relate to the competitive nature of the decarbonylation of ester vs. decarboxylation of carboxylic acid, illustrating how reaction kinetics are influenced by temperature, space velocity and gas dynamics, and thus highlighting the impact of residence time, diffusion and access to active site.

* Corresponding author at: Catalysis Science and Technology Research Centre (PutraCat), Universiti Putra Malaysia, 43400 UPM Serdang, Selangor, Malaysia.
** Corresponding authors.
E-mail addresses: kreem.alsultan@yahoo.com (G.A. Alsultan), nurul.asikin@ukm.edu.my (N. Asikin-Mijan), didikp@chem.its.ac.id (D. Prasetyoko), taufiq@upm.edu.my (Y. HinTaufiq-Yap).

https://doi.org/10.1016/j.fuproc.2026.108465
Received 16 March 2026; Received in revised form 21 April 2026; Accepted 22 April 2026
Available online 6 May 2026

1. Introduction

The global exponential growth of energy demand, coupled with the continued dependence of the electric power and transportation sectors on fossil energy sources, has increased the rise in the global mean surface temperature of the Earth. If effective methods for controlling this growth of energy demand are not forthcoming, the danger of a runaway greenhouse effect due to climate change is increased. This presents great danger of irreversible damage to the basic climatic systems of the Earth. These environmental stresses, coupled with the need for a more sustainable energy infrastructure, have resulted in an extensive worldwide effort to develop alternative fuels which will be renewable and carbon neutral. Among the myriad forms of renewable energy, feedstocks derived from biomass such as waste animal fats, waste vegetable oils and microalgal lipids are emerging as particularly attractive alternatives to fossil fuel-derived diesel, due to their natural abundance, inherent carbon neutral nature and compatibility with existing technologies for the production of liquid fuels [1,2]. Biomass-derived feedstocks are largely based on triglycerides (TGs), which are tri esters of glycerol and fatty acids. Such TG molecules can be converted to fuel-range hydrocarbons through various catalytic upgrading pathways. The traditional method by which TGs are converted to fuels is via transesterification to fatty acid methyl esters (FAME), which are currently the main components of biodiesel [3,4]. However, a general disadvantage of biodiesel is that is has undesirable physical and chemical properties such as low oxidative stability, poor cold-flow properties and incompatibility with existing fuel infrastructures. Another disadvantage of biodiesel is the large amounts of glycerol which are generated in the transesterification process which present numerous problems related to purification, valorization and process economics [5]. Consequently, these questions have prompted studies into various alternative upgrading routes with catalytic cracking/hydrocracking and catalytic deoxygenation leading to "green diesel", a new generation biofuel with chemical and physical properties similar to standard petroleum diesel, being of particular interest [6]. Green diesel is composed primarily of straight chain C_{15}–C_{18} hydrocarbons having boiling ranges similar to petroleum diesel and, importantly, has no aromatic components [7]. It therefore has performance properties similar to those of standard diesel fuel, but with a narrower boiling range distribution. More significant is the fact that green diesel fuel has a number of significant advantages over biodiesel, such as a higher heating value, higher energy density and cetane numbers (in the 80 to 90 range) which are exceptionally high owing to its paraffinic nature [8]. All these factors make green diesel an extremely attractive drop in fuel for use in present day compression ignition engines and warrants distribution on present day fuel distribution systems without any major changes being necessary.

The catalytic deoxygenation of triglycerides has therefore been the subject of great interest due to its efficiency in producing high yield and selective paraffinic green diesel product. Apparently, noble metal catalysts (for example, Pd on high surface area carriers) [9] showed effective in deoxygenation activity and selective towards green diesel, yet it usage is limited in their application due to their high cost, vulnerability (due to scarcity) and their (high) sensitivity to the oxygenated organic impurities present in biomass feeds [10]. The emphasis in research has therefore increasingly turned to research into transition metal catalysts for this process, of particular note being nickel catalysts, due to their lower cost, powerful hydrogenation capability and adequate deoxygenation performance [11]. Various formulations of Ni have been suggested that improve nickel performance such as supported Ni on palygorskite [12], Fe-promoted Ni catalysts which have high dispersion of metal particles [13], Pd-modified Ni/SiO_2–Al_2O_3 [14], bifunctional Ni/MgO–Al_2O_3 which have selective metal loadings [15], and ZSM-22 incorporated into the structure of Ni [16]. It has been shown that the support derived for a catalyst is a major modification of catalytic behavior as it affects most importantly not only the metal dispersion but the acid-base properties and even the catalytic redox performance. All of the supports available Al_2O_3 and ZrO_2 are two of those which are widely used as they have a high surface area, thermal stability and strong metal-support interaction [17]. From studies it was seen that Ni/ZrO_2 is better than both Ni/SiO_2 and Ni/γ-Al_2O_3 with regard to activity at low temperatures and the stability during the catalytic deoxygenation of WCO in a continuous fixed bed reactor [18]. Similar results on the synergistic effect found with Ni nanoparticles and ZrO_2 in the hydrodeoxygenation of fatty acids have been published by Zhao et al. [19]. On examining the mechanism of reaction, it was indicated by them that the carboxylic groups of fatty acids adsorbed preferentially on to the oxygen vacancies of ZrO_2 with the result that α-H abstraction was produced, with subsequent removal of oxygen leading to ketene intermediates, these being either hydrogenated or de-carbonylated at the nickel sites [20]. Furthermore, it has been shown that Ni supported on monoclinic ZrO_2 (Ni/m-ZrO_2) is much more catalytically active than on tetragonal ZrO_2 (Ni/t-ZrO_2), due to the greater concentration of oxygen vacancies present in the monoclinic form of ZrO_2 [21]. Changing the conditions of synthesis of Ni/ZrO_2 has also been shown to affect the electron density on the nickel, which allows for selective paths to deCOx products of hydrocarbons in the diesel range, such as n-heptadecane, to be obtained [22]. Recently, the successful doping of ZrO_2 with ceria (CeO_2) has shown to be an excellent method for improving catalytic behavior, due to the defect sites which appear from the introduction of substitution defects, the higher density of vacancy sites and altered redox properties of the support [23]. Ni-catalysts of different bimetallic systems Ni-Cu supported on ceria and ZrO_2 have also been reported by Yakovlev et al. [24] to possess a remarkable deoxygenation activity due to better activation of the oxygenated functionality produced on the surface of the support. There is however, still a huge scope for more improvement in activity, selectivity and long-term stability of the overall catalytic process to purify further green diesel from triglyceride-rich biomass taking place. Indeed, there is a need for use of profiling modelling tools judiciously for the evaluation of the effect of continually changing different reaction parameters, so that the reliance on the ever resource-wastefully experimental proof problems could be reduced somewhat. On the other hand, Sulfidated catalysts have received extensive attention for the de-oxygenation of palm oil and its derived products. This is mainly attributed to their good performances in deoxygenation. The transition metals used include conventional sulfids of nickel-molybdenum (Ni-Mo) and cobalt molybdenum (Co-Mo) that were anchored on gamma alumina (γ-Al_2O_3). These transition metal sulfides have exhibited good activities for deoxygenation(DO), decarboxilation (DCO) and decarbonilization (DCO_2) reactions. These reactions enabled the production of diesel range hydrocarbon by converting palm oil. $NiMoS_2$ based catalysts displayed higher than 75 wt% yield of C_{14} – C_{18} paraffin under optimal conditions. Therefore, these types of catalysts have shown great potential in the generation of green diesel from palm oil. The DO of waste oils using sulfided NiMo and NiW systems also show great deoxygenation activity and durability, however; the degree of degradation depends on the operational parameters and the chemical composition of the sulfided systems. Recently, it was found that the addition of Re in trimetallic sulfided catalysts (*Re*-Ni-Mo) improves the catalytic properties of the sulfided systems and increase the diesel yields, but also improve the resistance to coke formation during de-oxygenation process of palm oil. Despite their high activity levels, there are several challenges in the use of sulfided systems, i.e., loss of sulfur to the liquid phase, requirement of constant flow of sulfiding agents and sensitivity towards water generated during the reaction leading to reduction of the catalyst's life time and contamination of products. However, since their specific active site are linked to metal-sulfur phases and sulfur vacancy, sulfide catalysts remain a reference point for the most efficient de-oxygenation of palm oil and other triglyceride substrates [25–27]. Thus, the purpose of this study is to evaluate the catalytic deoxygenation of WCO using various Co and Mn-catalysts supported on Al2O3 in continuous fixed bed mode. Complete characterization studies (using XRD, N_2-physisorption, NH_3-TPD, CO_2-TPD, H_2-TPR, TPO, XPS FESEM

and HRTEM) have been made on all the catalysts, to highlight their physicochemical properties and active surface species which might be present, and the part played by the introduction of Co and Mn on their catalytic behavior. In parallel, some process modelling simulation (in theoretical mode) has been produced to check the findings of this experimental work and indicate the probable effect of some of the important parameters involved in its operation. The overall aim of the study is to show that the doping of MnS and CoS are an effective means of improving the catalytic behavior of the combined Mn-Co/AL2O3 systems effectively.

2. Materials and methods

2.1. Materials

All the materials used in this study were utilised as obtained from the vendor without additional purification. The chemicals, aluminum nitrate ($Al(NO_3)_3$) with 99.99% purity, Cobalt (II) nitrate hexahydrate ($Co(NO_3)_2{\cdot}6H_2O$) with 99.99% purity, Manganese (II) nitrate hexahydrate ($Mn(NO_3)_2\ 6H_2O$) with 99.99% purity, NaOH pellets with 99.99% purity were ordered from Sigma Aldrich (USA). High purity H_2S gas where supply by AGS Selangor Malaysia. Alkane and alkene comprised the liquid items; thus, a standard of *n*–(C_7–C_{20}) was applied to the GC analysis, with 1-bromohexane employed as the internal reference. Sigma Aldrich was also the source of the liquid standard GC grade n-hexane (Merck, Germany), which had a purity of over 98% and was utilised as the diluent. 99% pure nitrogen gas was obtained from Linde Sdn. Bhd. (Malaysia). Waste cooking oil (WCO) was used as the feedstock for the deoxygenation reaction was collected from a restaurant at Serdang, Selangor, Malaysia) and used without further purification. Table 1 summarises the fatty acid content of the WCO, included the saturated palmitic acid (45.68%), stearic acid (4.25%) and myristic acid (1.3%), together with the unsaturated oleic acid (40.19%) and linoleic acid (7.90%).

2.2. Catalyst preparation

The co-participation method was used in the catalyst preparation. Different solution concentration of each active side metals and the support were prepared separately. All metal precursor solutions were first combined using syringe pumps at a flow rate of 60 mL min^{-1} into 10 mL of deionized water under continuous stirring (600 rpm). This step was performed to ensure rapid and homogeneous mixing of Co and Mn ions prior to precipitation. After complete addition of the precursor solutions and subsequent mixing for 1 h to ensure uniformity, precipitation was initiated by the dropwise addition of 0.01 M NaOH at a controlled rate of 10 mL h^{-1} at room temperature. The slow addition of NaOH was employed to gradually increase the pH and control nucleation and particle growth. The resulting white precipitate was collected by centrifugation at 13,000 rpm, followed by repeated washing with deionized water until neutral pH was achieved to ensure removal of residual sodium ions. The samples were dried in oven at 100 °C for 24 h. The samples were grind in an agate mortar and pestle and then the samples were calcined in continuous air flow furnace with the heating rate of 5 °C per minutes and hold for 3 h at 550 °C and then cold down to 200 °C with a cooling rate of 10 °C per minutes then the H_2S gas were flow at 35 ml per minute and the furnace were heated to 600 °C with heating rate of 1 °C and hold for 3 h then the furnace were cooled down to room temperature naturally. The samples where labelled as $CoS_{(x)}MnS_{(y)}$/Al were x and y refer to the doping percentage (where x,y are 0.3 to 0.7 wt%).

Table 1
Properties of the waste cooking oil (WCO) used as the reaction feedstock.

Properties	Value
Density (g cm^{-3})	0.87
Viscosity (mm^2 s^{-1})	4.85
Moisture content (% wt)	1–5
Acid value (mg KOH g^{-1})	36.81
FFA content (%)	18.40
Fatty Acid composition	
Myristic acid, C_{14}:0	1.3%
Palmitic acid, C_{16}:0	45.68%
Stearic acid, C_{18}:0	4.25%
Oleic acid, C_{18}:1	40.19%
Linoleic acid, C_{18}:2	7.90%

2.3. Catalyst characterization

The identification of the crystallography and structural properties of all catalysts before and after the DO reaction was carried out using powder X-ray diffraction (XRD, Shimadzu, model XRD-6000). The XRD analysis was carry out with with a scan speed of 2°/min with a 2θ range within 2°–80°. The diffractograms that were produced were matched with the published International Centre for Diffraction Data (ICDD) files in order. The specific surface area and porosity of the catalyst were detected by using Brunauer-Emmett-Teller (BET) and Barrett-Joyner-Halenda (BJH) techniques (Thermo–Finnigan Shopmatic 1990 series N_2 sorption analyser). Degassing of the sample was performed overnight in 150 °C to eliminate any contaminating surface gaseous compounds and moisture on the catalyst surface. The adsorption and desorption process of N_2 were evaluated in a vacuum chamber at −196 °C. Temperature-programmed desorption with NH_3 as the probe molecules (TPD-NH_3) (Thermo-Finnigan TPDRO 1100, equipped with a corresponding thermal conductivity detector (TCD)), was employed to determine the acidic properties of the catalysts. 0.5 g of catalyst was added in the quartz tube, and the sample was pre-treated at 150 °C under N_2 conditions (30 mL min^{-1}) to remove excess moisture. The pre-treated samples were exposed to NH_3 for 1 h at room temperature for NH_3 adsorption. Subsequently, the excess NH_3 was flushed out using N_2 (20 mL min^{-1}) at room temperature for 35 min. The treated catalyst was heated from 50 to 900 °C at a heating rate of 10 °C/min in a flow of He (30 mL min^{-1}). The desorbed NH_3 was detected by the TCD. The H_2-TPR for reducibility species, TPO for spent catalyst and basicity of the catalyst were used the same TCD system by changing the probe gas into H_2, O_2 and CO_2, respectively. Prior to analysis, the TPD system was calibrated using pure NH_3 through ten injections to ensure consistent peak area and intensity, yielding a calibration factor of 8.601615×10^{-7} mmol mV^{-1} s^{-1}. A soda lime trap was installed to prevent water contamination. Finally, the temperature was maintained at 950 °C for 30 min to ensure complete desorption of NH_3 from the catalyst surface. Surface composition was analyzed by X-ray photoelectron spectroscopy (XPS) using a Kratos Axis Supra spectrometer equipped with a monochromatic Al Kα radiation source operated at an X-ray power of 180 W. Survey spectra were collected with a pass energy of 80 eV, while high-resolution spectra were acquired at a pass energy of 10 eV.

2.4. Catalytic activity evaluation

The deoxygenation (DO) reaction of the waste cooking oil (WCO) was carried out in a continuous fixed-bed reactor (Fig. 1) with approximately 10 g of catalyst was loaded at the center of the reactor and supported by 3 mm quartz particles, with quartz wool placed above and below the bed for stabilization and thermal insulation. To ensure the condition inside the reaction is inert, the system were been purged with inert N_2 gas, preheated to 150 °C and mixed with preheated WCO (110 °C) in a custom oil–gas mixing chamber. The resulting mixture was then introduced into a precision engineered 316 L stainless steel nozzle equipped with a 0.1 mm spray screen that provided precise atomization of the oil stream. The reaction temperature was monitored using four

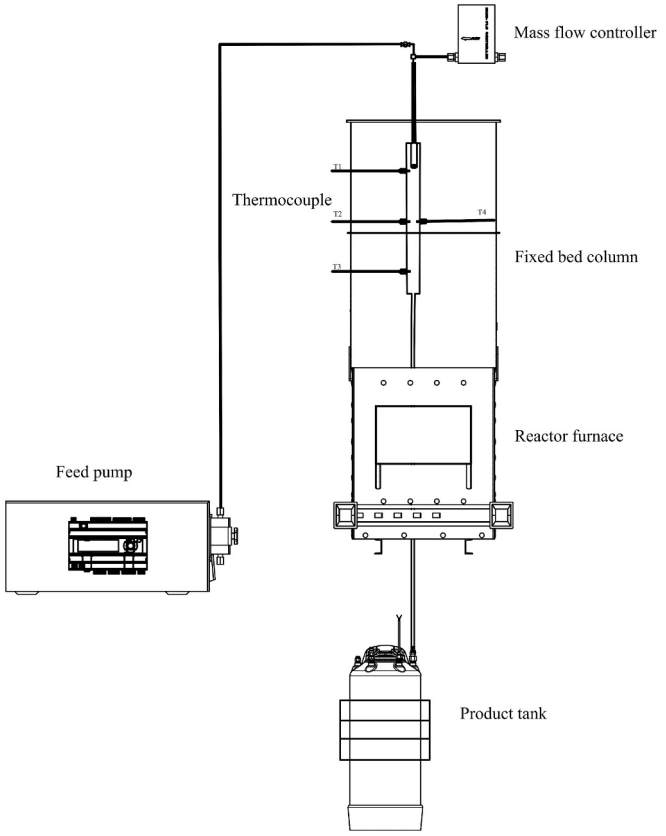

Fig. 1. Continuous deoxygenation reaction fixed bed reactor.

thermocouples connected to an eight-channel OMEGA data logger (OM-HL-EH-TC-K-CAL). The feed was delivered at a constant flow rate using a high-pressure HPLC syringe pump (Teledyne D-Series, Canada). Reactor effluents were condensed and collected in a receiver vessel, which was cooled to room temperature after each run via an external water-circulation system. Liquid products were analyzed by GC-FID and GC–MS.

2.5. Product analysis

The analysis of liquid products was carried out using a Shimadzu GC-14B gas chromatograph, using a HP-5 capillary column (30 m length; inner diameter, 0.32 mm; film thickness, 25 μm). The injector temperature of 250 °C and FID temperature of 300 °C was employed with He as a carrier gas with a flow rate of 30 ml/min. Samples for GC were prepared by adding 1 ml of *n*-hexane to dilute 1 μL of liquid product from the reaction, with 1 ml of 200 ppm of 1-bromohexane in hexane as an internal standard added for quantitative evaluation. The GC oven temperature was maintained at 40 °C for 6 min, then increased 7 °C every 6 min increments to a maximum of 270 °C. Both saturated and unsaturated hydrocarbon fractions, i.e., C_7–C_{20}, had been detected by GC–MS analysis previously. Thus, these were also assessed by GC-FID analysis with the use of reference materials obtained from industrial saturated hydrocarbons (C_7–C_{20}) and specially procured unsaturated nonene. The GC–MS and the calculation were reported in our previous publication [28,29].

3. Results and discussion

3.1. Characterization of synthesized catalysts

The surface morphology of the synthesized catalysts was examined by field-emission scanning electron microscopy (FESEM) (Fig. 2). The pristine Al_2O_3 support exhibits a layered and platelet-like morphology with compact structures and irregular stacking of alumina sheets. This type of morphology is common in calcined alumina and provides an asperous (rough) surface that enables the bonding and distribution of active metal species. When cobalt and manganese are incorporated by way of controlled coparticipation synthesis, notable morphological differences emerge. The FE-SEM images of the Co-Mn/Al2O3 precursor display irregular granular regions spread throughout the alumina structure. The presence of these granules indicate the successful nucleation and deposition of cobalt and manganese hydroxide precursor materials on the support surface. It is also probable that the use of syringe pumps to inject the precursor solutions reduced localized supersaturation conditions, enabling uniform precipitation of the metals throughout the alumina matrix. Upon sulfidization, the catalyst's morphology undergoes significant change. The sulfided CoS(*x*)MnS(y)/Al catalyst exhibits a fractured and aggregated nanostructure formed from small particulate domains located across the support surface. The particulates develop a “cauliflower” morphology as they form larger aggregates with nanometer scale dimensions. The development of this new morphology is due to the conversion of the oxide precursors to the sulfide phase during high temperature hydrogen sulfide treatment. High temperature sulfur treatments typically result in lattice rearrangements and volumetric expansions; these events may fracture the oxide domain structures creating smaller crystallite sizes within each sulfide phase. Therefore, it appears that the sulfidized aggregates are comprised of highly dispersed sulfide nanoparticles located on the alumina surface.

The high-surface-area and irregularly-porous structure of this nanoscale dispersion can be beneficial for catalytic reactions due to its increased exposure of the surface area which also results in an increase in the number of available active reaction sites. Furthermore, the dispersed particles' irregular shape and porosity should result in a faster rate of reactant/product diffusion into/out-of the particle during catalytic reactions. The HRTEM images of the Co–Mn/Al_2O_3 precursor show diffuse and poorly defined lattice fringes, suggesting the presence of small or partially amorphous oxide domains. This observation indicates that calcination at 550 °C produced highly dispersed metal oxides strongly interacting with the alumina support. Strong metal–support interactions can suppress the growth of large crystalline particles and stabilize finely dispersed metal oxide species. In contrast, the sulfided CoS(*x*)MnS(y)/Al catalyst exhibits well-defined lattice fringes, confirming the formation of crystalline sulfide phases after H_2S treatment at 600 °C. The enhanced lattice ordering indicates that sulfidation promotes crystallization of the active phase. The measured interplanar spacings obtained from the HRTEM micrographs correspond well with the crystallographic planes of cobalt sulfide and manganese sulfide phases. A lattice spacing of approximately 0.27–0.28 nm is assigned to the (100) plane of hexagonal CoS with a NiAs-type structure (JCPDS No. 65–3418). Another spacing of approximately 0.30–0.31 nm corresponds to the (111) plane of cubic MnS (JCPDS No. 40–1289). The lattice spacing values of approximately 0.18–0.19 nm for certain areas have been identified as possible evidence of both the (102) face of CoS and the (220) face of MnS. This identification further supports the transformation of metal oxide precursors into mixed metal sulfide nanocatalysts (CoS(*x*)MnS(y)) by confirming the presence of multiple faces in each individual catalyst particle. Additionally, the fact that all of the particles are at a nanoscale indicates that no agglomeration occurred due to the synthesis technique preventing interparticle sintering during high temperature treatment. Lastly, the simultaneous appearance of CoS and MnS domains indicates that heterometallic interfaces formed throughout the nanostructured catalyst. Heterometallic interfaces are well documented to alter the electronic environment of an active site and allow for enhanced performance through cooperative effects of both metals. Cooperative effects include charge distribution among the metals; improved surface area available for reactant adsorption; and creation of additional reactive sites due to either S vacancy or edge defect. Together, the FESEM and HRTEM data demonstrate that using a

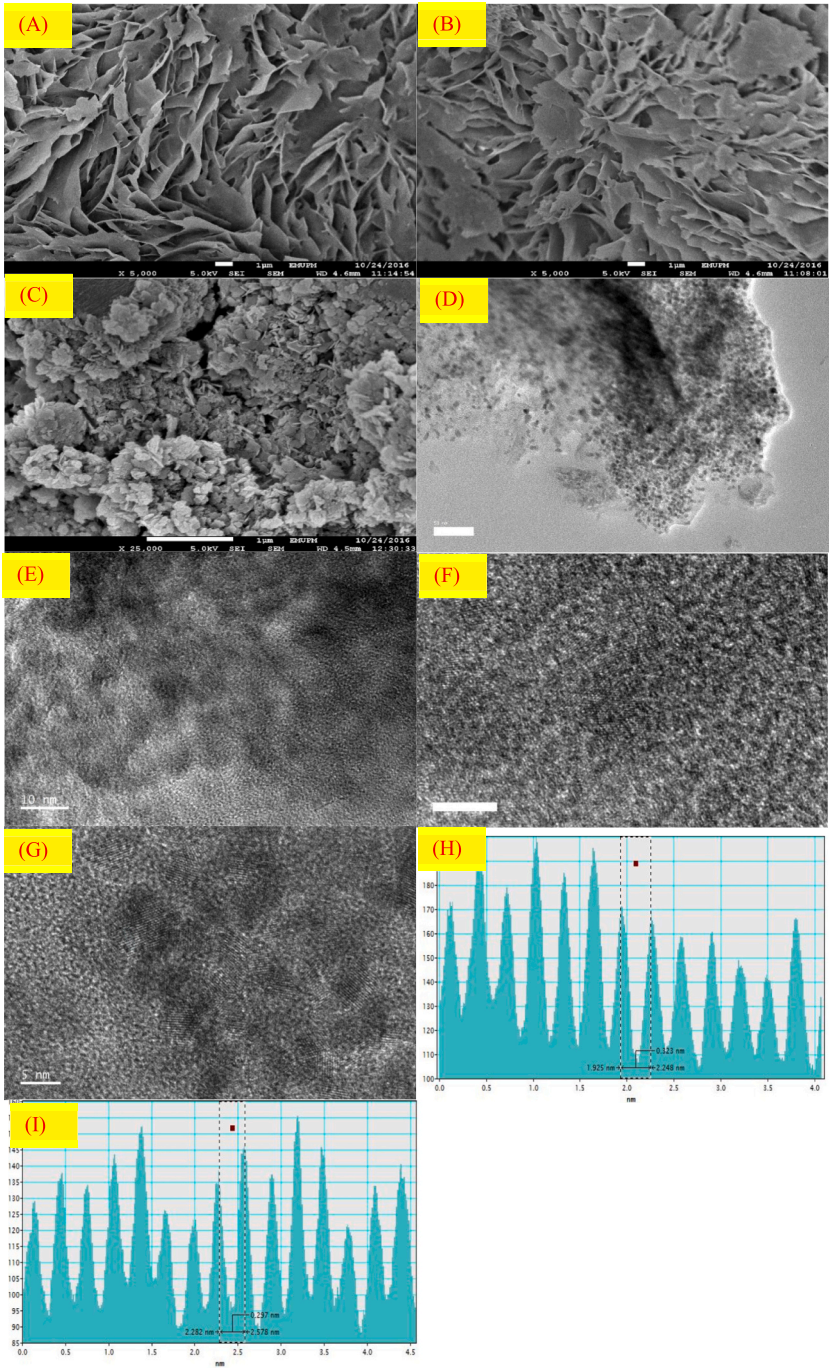

Fig. 2. FESEM results of (A) Al2O3, (B) Co–Mn/Al_2O_3, and (C) CoS–MnS/Al_2O_3 and HRTEM images of (D, E) Co–Mn/Al_2O_3, (F,G) CoS–MnS/Al_2O_3 after sulfidation, and (H,I) corresponding interplanar spacings before and after sulfidation.

co-sulfidation strategy allows for control over the co-participation of metals and results in a nanostructured CoS(*x*)MnS(y)/Al catalyst. The transition from layered alumina to uniform distributions of sulfide nanoparticles on a stable alumina support matrix illustrates how the active metals were successfully integrated into the overall structural design of the catalyst. As such, this unique architectural arrangement creates high densities of accessable active sites while maintaining structural integrity at elevated temperatures. Consequently, the catalyst structure is expected to promote efficient adsorption, electron transfer, and catalytic reaction kinetics.

The XRD was used to investigate the properties of the calcined catalyst within the 2θ range of 10^{o} –70_{o} with a particular peak based on the International Centre for Diffraction Data (ICDD). The XRD patterns of all catalysts are illustrated in Fig. 3, whereby the results confirms the formation of a multiphase catalyst comprising a γ-Al_2O_3–type support and sulfide phases derived from cobalt and manganese precursors. Aluminum Sulphide (Al_2S_3) Space group: R at 2θ 26.03°, 27.50°, 32.29°, 38.26°, 41.98°, 48.70°, 55.66°, 56.86°, 58.88° and 63.20° and hkl: (104), (110), (021), (024), (116), (300), (119), (220), (306) and (0210) with reference code: 00–047-1314 with crystal system of Rhombohedral. Reflections at 2θ ≈ 37.6°, 45.8°, and 67.3° are indexed to the (311), (400), and (440) planes of cubic γ-Al_2O_3, consistent with defect-rich transitional alumina rather than α-Al_2O_3 under the reference code: 00–001-1308. The moderate peak broadening indicates a nanocrystalline support with structural disorder typical of high-surface-area γ-Al_2O_3. Distinct reflections corresponding to rock-salt MnS

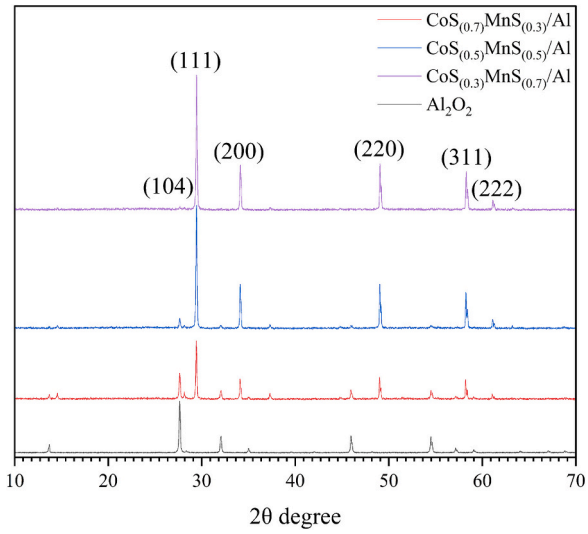

Fig. 3. XRD patterns of γ-Al_2O_3 support and Co—Mn sulfide/Al_2O_3 catalyst after H_2S sulfidation.

(alabandite) are observed at 2θ ≈ 29.5°, 34.2°, 49.1°, 58.4°, and 61.2°, indexed to the (111), (200), (220), (311), and (222) planes, respectively with Reference code: 01–072-1534. The relatively isolated MnS (111) reflection at ~29.5° provides clear evidence of Mn sulfidation. In addition, Linnaeite (ICSD: cubic Cobalt Sulphide (Co_3S_4)Space group: Fd_3m) 2θ: 38.10°, 50.07°, 64.67° and 68.99° and hkl: (400), (333), (533) and (444) with reference code: 00–002-1361, These results demonstrate effective sulfidation of both transition-metal species and the establishment of a MnS/Co_3S_4 heterostructure. Reflections attributable to rhombohedral Al_2S_3 are also detected, indicating partial sulfidation of the alumina surface under the applied conditions. Such interfacial revolution suggests O/S exchange at the metal–support interface, which may strengthen metal–support interactions and modulate surface acidity. However, excessive bulk conversion is not evident, implying preservation of the γ-Al_2O_3 structural backbone. Partial peak overlap is observed in the 37–40° and 48–50° regions due to contributions from γ-Al_2O_3, MnS, Co_3S_4, and Al_2S_3. Therefore, phase assignment was based on characteristic reflections in less congested regions together with whole-pattern analysis. The broader sulfide reflections relative to γ-Al_2O_3 suggest nanometric MnS and Co_3S_4 domains and possible interfacial microstrain, features that are typically associated with enhanced catalytic activity [30].

XPS results indicated both elemental composition on the surface and oxidation states of the various elements; thus, the successful conversion of metal-oxide precursors into the appropriate metal-sulfide phases and the resulting surface dispersions of the active species are demonstrated in Fig. 4A-E. The survey spectra show the expected photoelectrons signals for C 1 s, O 1 s, S 2p, Co 2p and Mn 2p, and there is no evidence of nitrate or organic precursors remaining, therefore, it can be concluded that all samples have been purified. Charge correction using the C 1 s peak at ~284.6 eV. The Co 2p spectrum shows a single major Co $2p_{3/2}$ component located at a binding energy typical of Co^{2+} in cobalt sulfide (CoS_x); this has also two satellites associated with shake-up transitions typical of divalent cobalt. There is no significant presence of Co^{3+} oxide species, confirming that the majority of cobalt is present in a sulfide form after H_2S treatment. Therefore, the reduction in binding energy relative to Co oxides formed through calcination in air at 550 °C along with the decrease in the intensity of the oxide related satellite peaks demonstrates that the sulfidation at 600 °C under flowing H_2S has successfully reduced the Co oxides to CoS_x. Similarly, the Mn 2p spectrum displays a Mn $2p_{3/2}$ peak located at a binding energy typical of Mn^{2+} in manganese sulfide (MnS_x). The major contribution to the Mn $2p_{3/2}$ peak is due to Mn^{2+} in manganese sulfide and there is only a very small contribution from higher binding energy components possibly attributed to either partially oxidized Mn or surface Mn-O-S moieties. As previously mentioned, calcination would produce Mn oxides (for example, Mn_2O_3/MnO_2), therefore, the almost complete predominance of the Mn^{2+} sulfide signal suggests that nearly all Mn oxides were reduced to MnS_x under these conditions. It should be noted that the slow heating rate (1 °C/min) could promote even sulfur diffusion throughout the structure and prevent sintering during phase transition. The S 2p spectrum presents a pair of doublets associated with S^{2-} species in metal sulfides. Only a weak shoulder is found at a high binding energy position, which may indicate minor amounts of oxidation (such as sulfate or sulfite species) occurring during air exposure. The predominant S^{2-} feature combined with a roughly stoichiometric S/(Co + Mn) ratio suggest that sulfur is largely coordinated in metal sulfide lattices and not as physisorbed H_2S or as surface sulfate layers. This would be consistent with a 3 h sulfidation treatment at 600 °C in flowing H_2S. The O 1 s region consists of components associated with lattice oxygen in alumina supports, hydroxyl groups on the surface and adsorbates. Rather than attempting to assign each component unambiguously, the O 1 s envelope may be considered to consist of a combination of oxygen derived from oxide- and hydroxyl-groups. The persistence of the O 1 s signal demonstrates that the oxide support remains intact and likely serves as a means of anchoring the sulfide nanoparticles and influencing the surface acid-base characteristics that influence deoxygenation catalysis.

The use of electron paramagnetic resonance (EPR) spectroscopy allowed us to identify the transition of metal-oxide precursors to metal-sulfides as shown by Fig. 5. Before sulfidization, there was little EPR activity associated with the catalyst which correlates to the predominately high-valent Mn^{3+}/Mn^{4+} and Co^{3+} species present in an oxide-based environment. High valence species in oxide systems usually have either broad or poorly defined signals resulting from both large zero-field splitting and strong antiferromagnetic exchange interactions; therefore, they are essentially silent when measured under typical EPR experimental conditions. After sulfidation, the EPR spectrum shows a marked increase in the amount of paramagnetic signal, and this indicates a substantial alteration in the electronic structure. There is a well-defined six-line pattern centered about g ≈ 2.0 as result of the hyperfine interaction with the ˆ55Mn ($I = 5/2$) nucleus. The observation of this pattern clearly identifies that Mn^{3+}/Mn^{4+} has been reduced to Mn^{2+}, and thus forms MnS. Additionally, after sulfidation, there is a broad and intense signal attributable to Co^{2+} in a tetrahedral sulfur-based ligand field. This signal is not seen in the metal-oxide precursor. The appearance of distinct Mn^{2+} and Co^{2+} signature patterns, along with increased signal intensity and characteristic g-values, indicates that the sulfidation process alters the local coordination environment of the metal centers. These observations are consistent with the formation of paramagnetic sulfide species with modified electronic environments. Thus, collectively, the progression from very weak, broadened signals related to the metal oxides to well-defined Mn^{2+} and Co^{2+} patterns provides definitive proof that MnS and CoS have formed within the catalyst system.

Catalytic sulfidation leads to a progressive loss of total NH3 adsorption capacity on gamma-Al2O3 as evidenced by TPD experiments. At the same time, there are significant qualitative and quantitative changes to the acid strength and number density of acidic sites available for reaction. In addition to the loss in overall acidity seen via the decreasing total NH3 adsorption capacities listed in Table 2, the TPD profiles indicate a complete restructuring of the acid strengths present [28,31]. As shown in Fig. 6, the original TPD profile obtained for pristine gamma-Al2O3 has been completely replaced after catalytic sulfidation. The original profile had a single broad TPD peak centered around 420 °C which was indicative of Lewis acid sites of moderate strength. These Lewis acid sites were generated by coordinatively unsaturated Al3+ ions. After sulfidation, all four catalysts have multiple peaks present, each centered over a range of temperatures. Additionally, each peak has an enlarged peak area compared to the original gamma-Al2O3 profile.

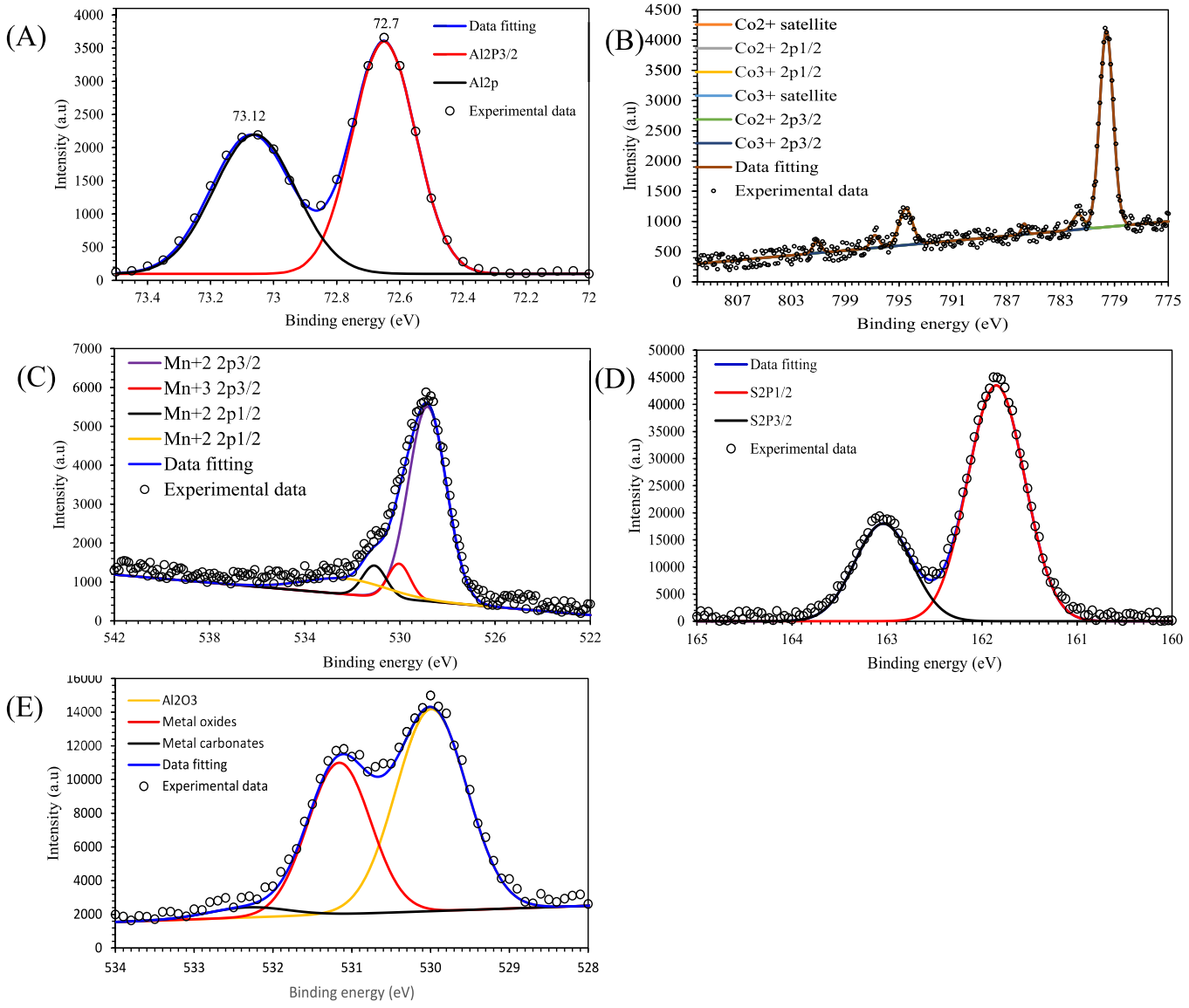

Fig. 4. XPS spectra of the Co-Mn catalyst showing Co^{2+}–S and Mn^{2+}–S species with a dominant S^{2-} doublet, confirming complete sulfidation and formation of active metal–sulfide phases for deoxygenation.

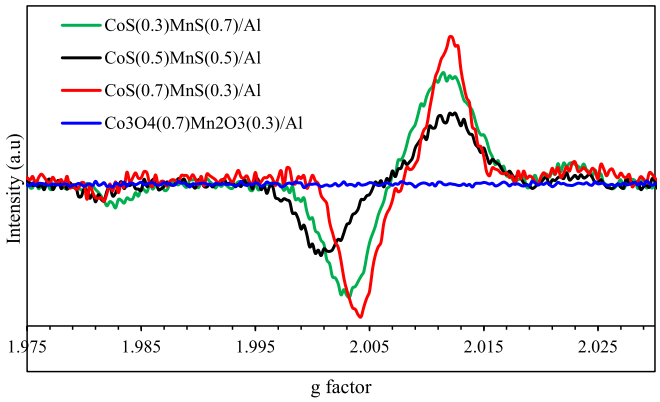

Fig. 5. EPR spectra of the catalyst before and after sulfidation confirming the formation of MnS and CoS phases.

Therefore, it can be concluded that the sulfidation process has resulted in a decrease in the strength of the Lewis acid sites originally found on gamma-Al2O3 [32]. However, there is also evidence that some or most of these original acid sites have become partially deactivated due to the formation of new acid sites. Since there is no evidence of acid-base pairs formed, it would appear that these new acid sites are being generated along the interface region between the support and the sulfided transition metals. In particular, CoS catalysts exhibit a series of low temperature desorption peaks which increase in size and intensity as the amount of CoS added increases. This is indicative of the presence of a large number of weakly acidic sites. For example, the 10% CoS sample has three distinct peaks; one centered near 300 °C and two larger peaks centered near 400 °C. These results suggest that CoS forms new, weaker Lewis acid sites at the interface regions of the support-metal system [33]. Although the exact nature of these new acidic sites cannot be precisely defined based upon these data alone, they do provide evidence for strong sulfide-support interactions and possible passivation of some or many of the high strength Lewis acid sites provided by the alumina substrate. On the other hand, MnS containing catalysts produce TPD profiles with significantly fewer peaks than those produced by their corresponding CoS analogues. Furthermore, the few peaks that are evident tend to occur at much higher temperatures than those observed for CoS containing samples. The increased peak temperature is

Table 2
the physicochemical properties of the prepared catalyst.

Sample code	XRD	N_2 absorption-desorption analysis		TPD-NH_3	
	Crystallite size (nm) (±0.5 nm)	Surface area ($m^2\ g^{-1}$) (±3)	Pore volume ($cc^3\ g^{-1}$) (±0.1)	NH_3 desorption temperature (°C) (±5 °C)	Total amount of NH_3 desorbed (μmol g-1) ± 1%
Al_2O_3	13.61	52.77	0.79	106/284/429	388.29
$CoS_{(0.7)}/Al$	15.54	39.15	0.72	329/422	1412.71
$MnS_{(0.3)}/Al$	14.70	41.09	0.74	117/391	1372.47
$CoS_{(0.3)}MnS_{(0.7)}/Al$	16.33	34.80	0.69	86/255/469	1864.93
$CoS_{(0.5)}MnS_{(0.5)}/Al$	17.58	28.79	0.61	93//286/444	2093.31
$CoS_{(0.7)}MnS_{(0.3)}/Al$	19.18	22.14	0.53	98/293/420	2821.69

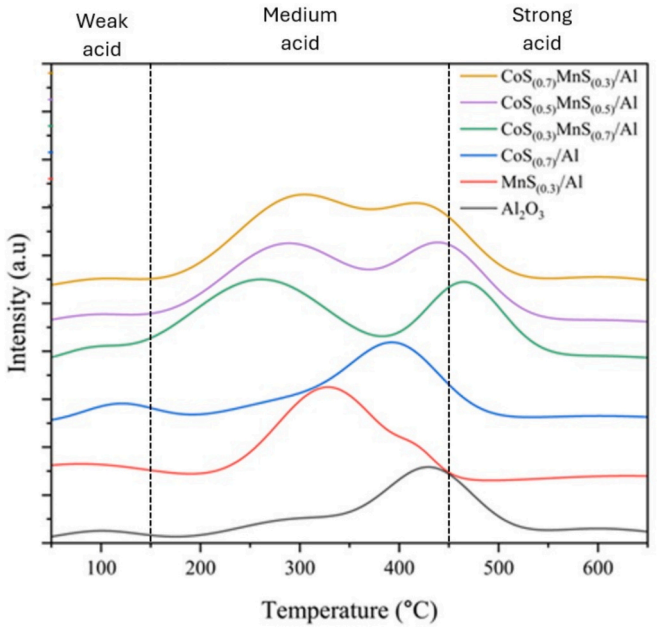

Fig. 6. NH_3-TPD profiles of Al_2O_3, MnS/Al, CoS/Al, and $Co_xMn_{1-x}S$/Al catalysts with varying sulfide loadings.

indicative of higher acid site strengths than those previously described for CoS. This behavior may be associated with modified metal–support interactions or changes in the local coordination environment at Mn-containing interfaces. These high strength sites will be discussed further below. Finally, mixed Co0.5Mn0.5S catalysts show what could best be termed as "synergistic" effects with respect to controlling acidity levels. Specifically, CoS enhances site density, while Mn-containing catalysts exhibit higher NH_3 desorption temperatures, suggesting the presence of relatively stronger adsorption sites. However, NH_3-TPD alone does not allow definitive assignment of the nature or origin of these sites. Of course, it is impossible to know whether this synergism arises from direct interactions between Co and Mn Sulfide phases or if such interactions arise solely due to differences in sulfide phase dispersion across the support surface. Regardless of its origin however, this synergy allows for creation of an optimal acidity profile [34]. The optimal Co/Mn ratio for this synergetic effect is clearly demonstrated by the fact that Co0.5Mn0.5S preserves mesoporosity and balances moderate-strong acidity levels.The TPD profiles of the Mn-based composite catalysts show a very high number of weak to medium acid sites; evidence for this is the major desorption peak at those locations (see Fig. 6). Based on this analysis, it can be deduced that the total acidity contributed from the combination of Mn and Co species has decreased while the ratio of weak to medium acid site is significantly increased when Al_2O_3 was incorporated into the material. Thus, changes in acidity are expected to lead to improved catalytic behavior and reduced coke deposition under reaction conditions [35,36].

Table 2 shows the BET surface area of Al_2O_3 ($52.77 m^2\ g^{-1}$) has reduce drastically to $39.15\ m^2\ g^{-1}$, $41.09\ m^2\ g^{-1}$ $34.80\ m^2\ g^{-1}$, $28.79\ m^2\ g^{-1}$ and $22.14\ m^2\ g^{-1}$ for CoS $_{(0.7)}$/Al, MnS $_{(0.3)}$/Al, $CoS_{(0.3)}MnS_{(0.7)}$/Al, $CoS_{(0.5)}MnS_{(0.5)}$/Al and $CoS_{(0.7)}MnS_{(0.3)}$/Al catalysts, respectively. Similar case with pore volume of all samples which are gradually reduced once the Al_2O_3 support was incorporated with CoS and MnS. The reduction in pore volume was due to the excess of active metals embedded into the channel of parent materials and incorporated into the pore of Al_2O_3 [37]. The reduction of surface area of all catalysts are concomitantly with large particle size of aggregates which composed of large crystallite size. N_2 adsorption–desorption isotherms reveal a progressive transition from mesoporous γ-Al_2O_3 (type IV isotherm Fig. 7) to increasingly pore-filled sulfide composites with rising metal loading. Pristine Al_2O_3 exhibits pronounced capillary condensation at $P/P^0 \gtrsim 0.9$, indicative of well-developed mesoporosity. Incorporation of CoS and MnS systematically reduces total adsorption volume and narrows the hysteresis loop, reflecting partial pore filling, neck constriction, and decreased accessible surface area. The effect is most pronounced in Mn-rich and highly loaded bimetallic samples, consistent with sulfide crystallite growth within pore walls and partial blockage of smaller mesopores [38]. The X-ray diffraction (XRD) analysis indicates that there is gamma alumina and manganese sulfide (alabandite), cobalt(II) thiospinel (linnaeite), and aluminum sulfide at the interface formed during the partial oxidation of the alumina support. This suggests that the alumina was partially oxidized and converted into other phases; i.e., aluminum sulfide. The XRD results also indicate that nanoscale domains of alabandite (manganese sulfide) and linnaeite (cobalt(II) thiospinel) are present on the surface along with aluminum sulfide formed at their

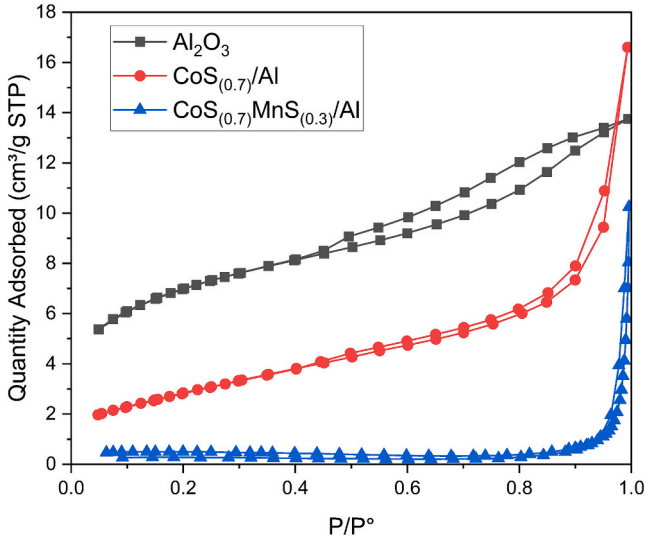

Fig. 7. Nitrogen adsorption–desorption isotherms of Al_2O_3, $CoS_{0.7}/Al$, and $CoS_{0.7}MnS_{0.3}/Al$ catalysts measured at 77 K. The decrease in adsorbed N_2 volume after metal sulfide deposition indicates partial pore blocking and reduced accessible surface area compared with the pristine Al_2O_3 support.

interfaces. These nano-domains are responsible for the reduction in pore size and decrease in surface area. The changes made to the pore structure will be reflected in the number and type of surface acidic sites available on this material. Acidic site distributions were investigated through temperature-programmed desorption of ammonia (NH_3-TPD). The data show that the CoS-rich samples have larger numbers of relatively weak to moderately strong surface acidic sites than the MnS-rich samples (See Fig. 6). The differences in acidic site strength can be related to the different types of chemical bonding present in these two samples. Specifically, Co–S–Al interfacial bonding contributes to many of the weak to moderately strong acidic sites. On the other hand, MnS-rich samples contain a large number of stronger Lewis-acidic sites resulting primarily from the presence of highly polarized Mn—S bonds and Mn–S–Al linkages. Samples containing both CoS and MnS display an intermediate acidity profile that balances both site density and strength. It has been demonstrated that both the structural properties and the acidic properties of a supported metal sulfide determine how it functions in converting organic matter such as waste-cooking-oil (WCO) into products such as renewable diesel fuel [39,40]. For example, CoS-rich samples possess adequate mesoporosity to allow for easy access to reactants, while possessing an appropriate level of acidity to promote controlled hydrodeoxygenation reactions. As a result, they produce a higher yield of hydrocarbons in the range of C_{15}-C_{18}. Increasing the amount of MnS in the sample increases its acidity and enhances its ability to promote decarboxylation and/or decarbonylation reactions which lead to higher levels of CO/CO2 production and greater cracking propensity. The best performance was observed when there was a good balance between Co and Mn. A good balance exists because there is enough mesoporous space for large molecules such as triglycerides to enter but still provides a high concentration of electronically active sulfide edge sites for efficient cleavage of C—O bonds. Therefore, an understanding of how the structural properties and acidity properties work together to determine how efficiently a given organic substrate can be converted into desired products is essential for rationally designing sulfide-based catalysts with suitable combinations of porosity and acidity to effectively convert biomass-derived feedstocks into renewable fuels.

The adsorption of pyridine on the sulfided CoS0.50-MnS0.50/Al2O3 catalyst results in an increase in surface acidic properties compared to those observed for the corresponding oxide form of this material (CoSx-Mnx/Al2O3). The presence of two intense bands at 1403 and 1659 cm-1 in addition to several weaker bands at approximately 1530–1535 and 1621–1633 cm-1 are indicative that both Brønsted acid sites capable of coordinating pyridinium ions and Lewis bound pyridine are present (see Fig. 8) [41]. These bands are absent or very weakly represented in the IR spectrum of the non-sulfurized Co-Mn/Al2O3 catalyst. Additionally, it has been demonstrated that the high degree of Brønsted acidic character exhibited by the Co-S/Mn-S/Al2O3 system is due to changes in the chemical state of the sulfur atoms and the metallic centers as well as the creation of new sites which can act as H+ donors and coordinately unsaturated sites which can bind pyridine [42,43]. Bands attributed to pyridinium ions indicate the presence of proton-donating sites, which may originate from surface hydroxyl groups or interfacial metal–sulfur–support interactions rather than classical sulfide Brønsted sites. The existence of these two types of acidity contributes significantly to the enhanced performance of the Co-S/Mn-S/Al2O3 catalyst for the deoxygenation of palm oil. While Lewis acids facilitate the activation of oxygenated functional groups such as carbonyls and esters thereby favoring hydrodeoxygenation; Brønsted acids accelerate the scission of carbon-carbon bonds and carbon-oxygen bonds during decarboxylation and decarbonylation processes respectively. Thus, the sulfided Co-S/Mn-S/Al2O3 catalyst is anticipated to have greater deoxygenation activities than its oxide counterpart and be able to produce a higher proportion of longer chain paraffins in the "green" diesel boiling range.

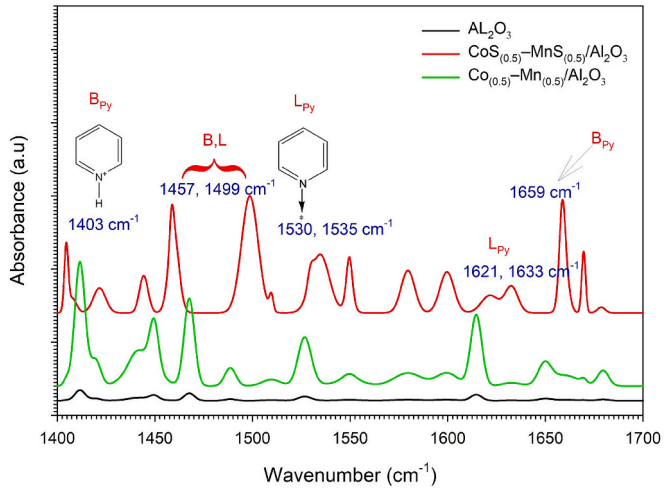

Fig. 8. FTIR–pyridine spectra showing Brønsted and Lewis acid sites of Al_2O_3, $Co_{0.5}$–$Mn_{0.5}/Al_2O_3$, and sulfided $CoS_{0.5}$–$MnS_{0.5}/Al_2O_3$.

Table 3 highlights the interplay between sulfide composition, acidity, structure, and deoxygenation performance. Pristine gamma-Al_2O_3 has moderate-strength Lewis acid sites with a relatively low number of active sites; has many pores (mesoporosity); and little deoxygenation capability. It is capable of converting less than 1% of the feedstocks into product and has very little ability to crack larger molecules. When cobalt was incorporated into the alumina and formed CoS/Al there were more Lewis acid sites present on this material than pristine gamma-Al_2O_3 [29,44]. However, the cobalt incorporation resulted in lower average strengths for these acid sites. One reason for the weaker acid sites is due to the presence of Co_3S_4 units. Another reason is that when cobalt was incorporated into the alumina it caused some aluminum to react with sulfur to form Al_2S_3 at the interface of the two phases. Therefore, the CoS/Al phase can selectively undergo hydrodeoxygenation (HDO), which enhances the formation of heavier paraffinic products (C_{15}-C_{18}) and suppresses gas formation. In contrast, the MnS/Al phase contains fewer Lewis acid sites than CoS/Al but each one is stronger because of the interaction of manganese with both sulfur and aluminum. As such, these acid sites are conducive to decarboxylation/decarbonylation (DCO/DCO_2). Therefore, MnS/Al produces a greater amount of lighter paraffinics (C_{14}) as well as a greater amount of CO and CO_2 byproducts. Additionally, since these acid sites are so strong they may lead to secondary cracking, which reduces liquid yield and catalyst lifetime. Because bimetallic Co-Mn sulfides allow for tuning of acidity and subsequent reaction pathways, a range of materials could be synthesized. Specifically, $Co_{0.7}Mn_{0.3}S$/Al exhibited intermediate acidity along with moderate pore constriction. Thus, the resulting material demonstrated a balanced mix of DCO and DCO_2 activity. A material with even higher levels of acidity ($Co_{0.3}Mn_{0.7}S$/Al) would exhibit enhanced DCO compared to DO; would produce more gas; and would result in decreased catalyst stability. Therefore, the findings clearly illustrate that an ideal balance of acid strength, site density, and structural integrity – most successfully achieved with $Co_{0.5}Mn_{0.5}S$/Al – is essential to achieve maximum deoxygenation efficiency; retain liquid fuel selectivity; and enhance catalyst life.

3.2. Deoxygenation reaction of WCO

A strong correlation exists for deoxygenation (DO) of waste cooking oil (WCO), depending upon reaction time, catalyst composition, temperature, Whipple-Hoffmann Space Velocity (WHV), and nitrogen flow rates (Fig. 9). Maximal green diesel yields (85–90%) were achieved in the first hour at full site availability, allowing for rapid conversion of triglycerides and FFAs into hydrocarbons having a carbon number range of 15–18 through cooperative decarboxylation/decarbonylation (DCO/DCO2) and hydrodeoxygenation (HDO) processes. Over the second –

Table 3
Relationship between sulfide composition, acidity, structural properties, and deoxygenation performance.

Catalyst	Acidity Trend	Acid Strength	Acid Density	Structural Interpretation (BET and XRD)	Expected Deoxygenation Pathway	Performance Implication
Al_2O_3	Baseline Lewis acidity	Medium	Low	High mesoporosity; no sulphide domains	Mild DO	Limited activity; minimal cracking
CoS/Al	More sites but weaker	Low–Medium	High	Partial pore blocking; Co_3S_4 formation; some Al_2S_3 interfacial sites	DO-favoured	Higher C_{15}–C_{18} paraffins; lower gas formation
MnS/Al	Fewer but stronger	High	Medium	Strong Mn–S–Al sites; higher micro strain	DCO/DCO_2-favoured	More C_{14} products; higher CO/CO_2; risk of cracking
$Co_{0.7}Mn_{0.3}S$/Al	Balanced acidity	Medium–High	Medium–High	Moderate pore narrowing; synergistic Co_3S_4–MnS phases	DCO	Balanced paraffin selectivity and activity
$Co_{0.5}Mn_{0.5}S$/Al	Optimal compromise	Medium	High	Good dispersion; preserved mesoporosity; reduced blocking	Highly efficient DO	High conversion, minimized cracking and coke
$Co_{0.3}Mn_{0.7}S$/Al	Strong acidity dominates	High	Medium	Greater pore blockage; MnS-rich interfaces	DCO-leaning with cracking risk	More gaseous products, faster deactivation

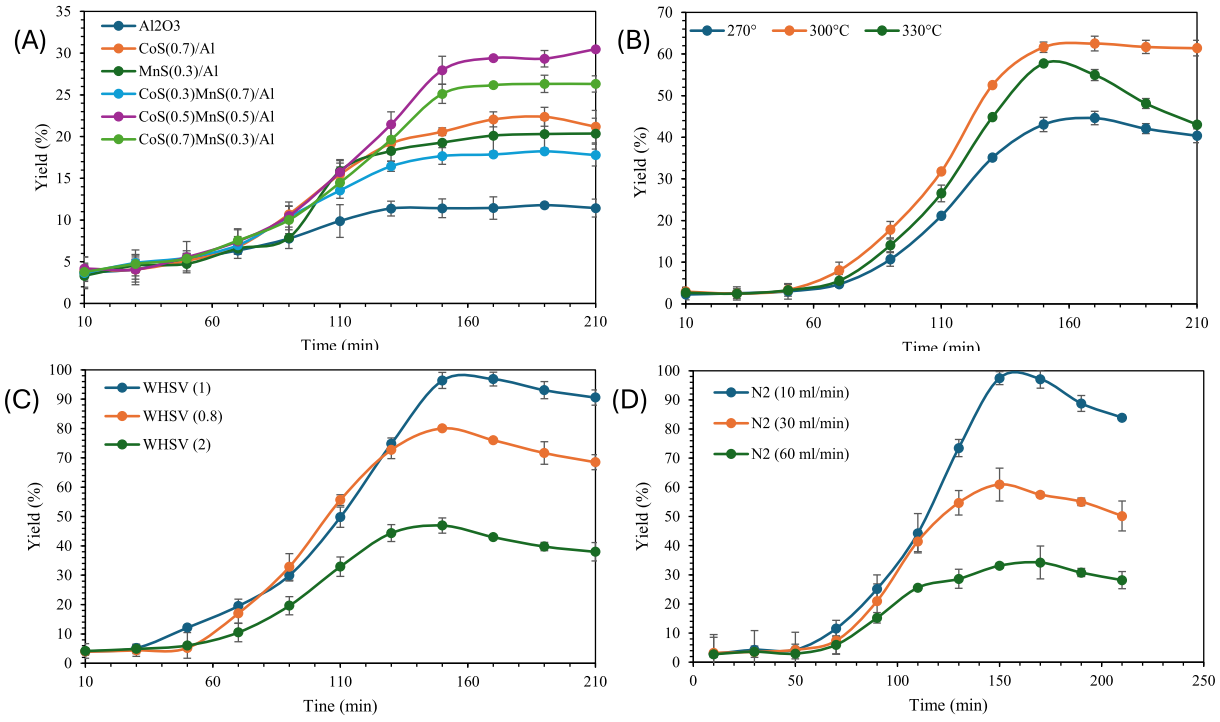

Fig. 9. DO of WCO over CoS–MnS/Al_2O_3 catalysts: (A) catalyst screening at 270 °C, WHSV = 1 h^{-1}, N_2 flow = 10 mL min^{-1}; (B) effect of reaction temperature on $CoS_{0.5}$–$MnS_{0.5}$/Al at WHSV = 1 h^{-1}, N_2 flow = 10 mL min^{-1}; (C) effect of WHSV on $CoS_{0.5}$–$MnS_{0.5}$/Al at 300 °C, N_2 flow = 10 mL min^{-1}; (D) effect of nitrogen flow on product yield at 300 °C, WHSV = 1 h^{-1}.

third hour, yields declined to 75–80% due to partial site deactivation resulting from the build-up of coke deposits on active sites, as well as water and CO/CO2 adsorption onto active sites. Additionally, during this time frame an increase in O-containing intermediates accumulated on sites, thereby restricting access to both metal and acid sites and influencing selectivity towards partially converted species. By the fourth – fifth hours, there was extensive site deactivation as well as pore plugging that resulted in decreased yields of 60–70%. During this period, it became apparent that secondary cracking had occurred to produce lighter hydrocarbon products (C8-C14) along with additional gaseous products. After six hours, a steady state condition was observed where the yield remained relatively constant at approximately 50–60%, indicating that sites previously deactivated were now redistributed such that preferential decarboxylation of FFAs and triglycerides was occurring over hydrodeoxygenation. In addition, during this time frame, there was a loss of selectivity to C17-C18 hydrocarbons. These results indicate that periodic regenerations of the catalyst will be necessary as well as optimizing the WHV and controlling either hydrogen or nitrogen feed rates to extend the useful life of the sulfide active sites. The composition of the catalyst significantly influences the mechanisms involved in deoxygenation. The pristine Al2O3 exhibits moderate Lewis acidity and has limited numbers of sites available for catalysis. As a result, only mild levels of deoxygenation are exhibited. Increasing the acid site density by adding CoS to form Co3S4 and Co-S-Al interface sites decreases the strength of the acidic sites. This promotes primarily hydrodeoxygenation to C15-C18 paraffin products with limited amounts of cracking. Increasing the acid site strength by incorporating MnS into the Al2O3 supports fewer but stronger sites from the interaction of Mn-S-Al. This favors greater DCO/DCO2 pathway activity, CO/CO2 production, and C14 hydrocarbon production. However, these factors also contribute to a greater potential for secondary cracking and shorter catalyst lifetime. The bimetallic Co-Mn sulfides provide a means of tuning properties. For example, Co0.7Mn0.3S/Al exhibits an intermediate level of acidity and porosity that balances DCO and DCO2 behaviors. Also, Co0.5Mn0.5S/Al optimizes the combination of maximum acid site density, moderate site strength, and minimum mesoporosity restriction for maximal green diesel yield and minimizing coke formation. Conversely, higher Mn content (e.g., Co0.3Mn0.7S/Al) produces

more acidic sites and increased pore clogging that promotes greater DCO than DO pathways and enhances gas production at the expense of catalyst durability. Temperature governs kinetic rate and product distribution. Optimal temperatures (>300 °C) support the most efficient breaking of C—O bonds and conversion of triglycerides to diesel-range hydrocarbons. Temperatures above optimal values enhance secondary cracking to light products. Residence times can be modified using WHV: lower WHV maximizes complete removal of oxygen and hydrogen atoms from triglycerides and FFAs, thereby maximizing C15-C18 hydrocarbon yields; conversely, higher WHV limits contact time leading to intermediate buildup and subsequent loss of green diesel yield. Nitrogen flow regulates partial pressure of reactants/products: moderate flow (~10 mL minˆ-1) minimizes water, CO, CO_2 adsorption onto active sites resulting in less coking/blocking; conversely too low flow rate limits conversion; too high flow rates limit retention times leading to reduced selectivity. Overall, the bimetallic CoS-MnS system clearly illustrates that maintaining an optimal balance between sulfide composition, acidic site strength/density, structural porosity, and reaction conditions are required to achieve high efficiency WCO deoxygenation producing high yields of C15-C18 hydrocarbons while minimizing secondary reactions and ensuring long-term catalyst stability under hydrogen lean conditions.

The time-dependent evolution of green diesel yield was used to evaluate the apparent kinetics of product formation over the $CoS_{0.5}$–$MnS_{0.5}/Al_2O_3$ catalyst at different reaction temperatures (Fig. 10). Among the tested kinetic models, the zero-order model provided the best fit to the experimental data (R^2 = 0.87–0.93), indicating that the formation rate of green diesel is independent of the reactant concentration and controlled by surface reaction kinetics under conditions of catalyst site saturation. The apparent rate constants increased from 2.32×10^{-3} min^{-1} at 270 °C to 3.37×10^{-3} min^{-1} at 300 °C, confirming the accelerating effect of temperature on hydrodeoxygenation activity. At 330 °C, a lower apparent rate constant (2.84×10^{-3} min^{-1}) was observed, which is attributed to the onset of secondary cracking and over-hydrogenolysis reactions leading to partial degradation of the green diesel fraction. The apparent activation energy estimated from the kinetically controlled region (270–300 °C) was 32.2 kJ mol^{-1}, which falls within the typical range reported for hydrodeoxygenation reactions over sulfided transition-metal catalysts.

3.3. Characterization of Spent $CoS_{(0.5)}MnS_{(0.5)}/Al_2O_3$ Catalysts

XRD analysis of fresh $CoS_{0.5}MnS_{0.5}/Al_2O_3$ shows reflections of γ-Al_2O_3 (2θ ≈ 37.6°, 45.8°, 67.3°) and well-defined metal sulfides, MnS (2θ = 29.5°, 34.2°, 49.1°, 58.4°, 61.2°) and Co_3S_4 (2θ = 38.1°, 50.1°, 64.7°, 69.0°), confirming structural integrity of the support and successful formation of crystalline Co-Mn sulfide active domains (Fig. 11A). After WCO deoxygenation, the spent catalyst retains these principal reflections, indicating the bulk framework remains stable and deactivation is not due to phase collapse. However, broad diffuse humps at 2θ ≈ 20°, 38°, and 59° appear, characteristic of amorphous carbon from secondary cracking, condensation, and polymerization of reactive intermediates. These carbonaceous deposits preferentially accumulate on accessible Co-Mn sulfide sites, blocking surface activity and pore mouths, which limits reactant adsorption and diffusion of bulky triglycerides. The diffuse nature of these deposits reduces the apparent intensity of sulfide reflections without altering the crystalline phases. Oxidative TGA confirms carbon deposition as a primary deactivation mechanism, indicating the catalyst remains regenerable under oxidative treatment.

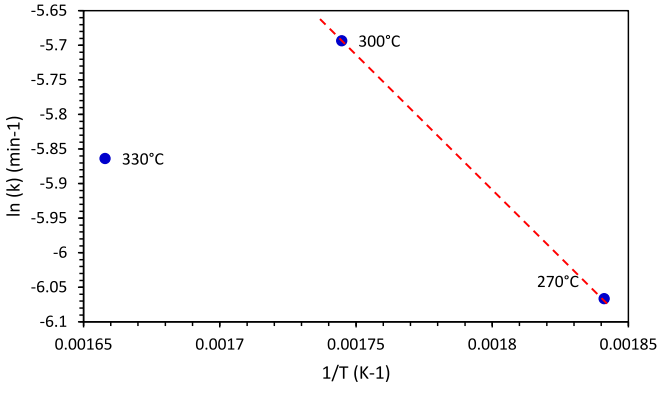

Fig. 10. Arrhenius plot (ln (*k*) lnk vs. 1/*T*) for the apparent green-diesel formation rate constant during palm-oil deoxygenation over $CoS_{0.5}$–$MnS_{0.5}/Al_2O_3$. The activation energy was calculated from the linear region between 270 and 300 °C. (For interpretation of the references to colour in this figure legend, the reader is referred to the web version of this article.)

Fresh and used CoS0.5MnS0.5 / Al2O3 by thermogravimetry (TG) in O2 atmosphere (see Fig. 11B) exhibit a complex degradation process due to various steps including desorption, oxidation of sulfides and combustion of residual carbon. Moisture and volatile compounds are released prior to 200 °C from both the new and used catalyst. The two catalysts show similar weight loss up to approximately 400 °C, but the used catalyst has larger mass loss above this temperature; which corresponds to an increased oxidative decompostion of organic intermediates and volatile light organics. Slightly less than half of the total weight loss for each sample is observed between 400 and 580 °C, where CoS and MnS have been oxidized to their respective oxide forms with simultaneous release of SO2 and complete combustion of all the strongly bonded carbon. Importantly, there was significant mass loss (~8 wt%) for the used catalyst at temperatures higher than 580 °C, which indicates partial coke formation as a result of the deoxygenation of WCO. The relatively low level of coke present demonstrates that the CoS-MnS metal alloy system supported on alumina does not significantly inhibit oligomerization of oxygen-containing molecules into solid polymers. Additionally, since the TG data indicate no sharp peaks in mass loss after 580 °C, it can be inferred that most of the coke is soft (reactive). Therefore, these results confirm that the catalyst is thermally stable and resistant to coke formation, making it suitable for use in multiple sequential WCO hydrotreating reactions to produce renewable diesel fuel.

4. Comparison study

A comparison study presented in Table 4 shows that lipid based feedstocks (coconut oil, palm oil, palm kernel oil and palm fatty acid distillate PFAD) outperform lignocellulose biomass for the development of sustainable aviation fuels (SAF) and green diesel. Hydrocarbon yields and jet fuel range selectivities generally can be obtained by using low pressure hydrogen (moderate to 50 bar) at temperatures ranging from 320 to 400 °C and performing either catalytic deoxygenation or hydrodeoxygenation. For example, when triglycerides are converted using transition metal catalysts (such as nickel, nickel cobalt, and nickel molybdenum) yields of greater than 70–90% of hydrocarbons were achieved and these hydrocarbons had a carbon number of 9–18 which is well-suited for use as an aviation fuel. The conversion of lipid feedstock into hydrocarbon fuels was shown to occur via decarboxylation, decarbonylation, and/or hydrodeoxygenation of the long chain fatty acids found within the triglycerides.

The properties of the catalyst (composition and microstructure) also affect both the yield and distribution of hydrocarbons. Bimetallic catalysts (for example Ni-Co or Cu-Ni) have been reported to offer better performance than monometallic Ni catalysts due to synergetic effects between metals, higher dispersion of active sites, and larger surface areas. However, even though monometallic Ni catalysts do not provide the same level of synergy they still represent the most cost effective option and thus continue to dominate this reaction. Catalysts derived from MOFs can offer additional advantages over traditional supported metal catalysts. Additionally, some acidic supports (for example zeolite)

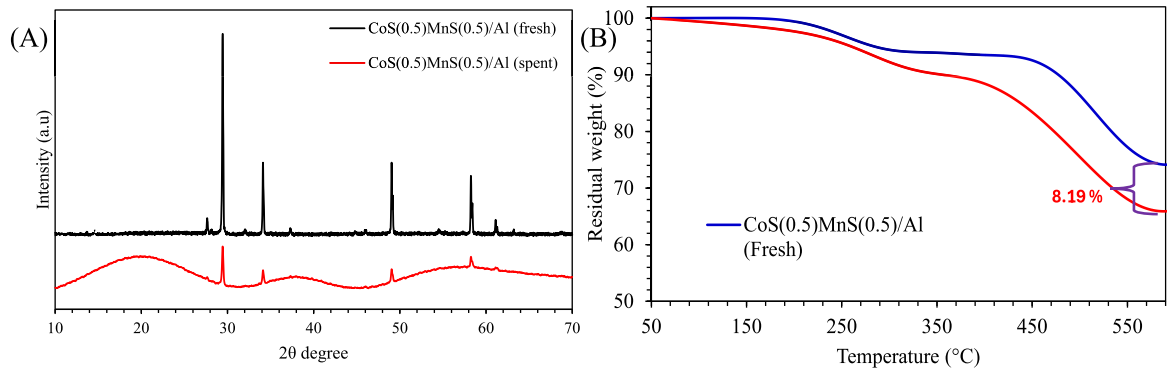

Fig. 11. (A) The XRD patterns of the fresh and spent CoS(0.5)MnS(0.5)/Al catalysts before and after the deoxygenation reaction and (B) TGA profiles of the fresh and spent $CoS_{(0.5)}MnS_{(0.5)}$/Al catalysts recorded under an oxygen atmosphere.

Table 4
comparison study with previous published work.

Feedstock	Catalysts	Operating Conditions	Results	Reference
Coconut oil	Ni/ZIF-67 derived Co-C (1–10 wt% Ni)	350 °C, 4 h, 30 bar H_2	Hydrocarbon yield 99.01%, jet-paraffin selectivity 91.61%	[47]
Palm kernel oil (PKO)	$NiCo/Fe_3O_4$	350 °C, 3 h, 5 wt% catalyst	Hydrocarbon yield up to 90%, kerosene fraction >90%	[45]
Palm kernel oil	$Ni_{0.5}Co_{0.5}/Fe_3O_4$	350 °C, 3 h, N_2 atmosphere	Hydrocarbon selectivity ≈91%, BJF fraction ≈95%	[48]
Palm oil	Nb_2O_5	350 °C under N_2	Deoxygenation efficiency 89%, SAF fraction 64–67%	[49]
Macauba oil	CaO derived from eggshells	Catalytic pyrolysis, N_2 atmosphere (~10 bar)	Hydrocarbon liquids ≈95 wt%, cyclic hydrocarbon selectivity 13%	[46]
Palm oil	Ni/AC–Al_2O_3	400 °C, 3 h	SAF-range alkanes 70.6%, selectivity 77.2%	[50]
Empty fruit bunch (EFB) + polypropylene	NiFe/ZSM-5	Pyrolysis 400–600 °C	Improved liquid fuel yield and hydrogen-rich gas formation	[51]
Palm kernel shell + fresh palm fruit	Non-catalytic pyrolysis	550 °C (double auger reactor)	Bio-oil yield 17.4%, diesel fraction 33%	[52]
Fresh palm fruit bunch	Slow pyrolysis	400–600 °C	Optimal oil yield 21.9% at 500 °C	[53]
Palm oil	NiMo/Al_2O_3, NiMo/HZSM-5, NiMo/ZrO_2 with glycerol as H-donor	Catalytic deoxygenation process	Oxygen removal up to 74.3%, catalyst support strongly affects product distribution	[54]
Palm empty fruit bunch	Hydrothermal liquefaction (HTL) with ethanol co-solvent	275–300 °C, 30 min, 10 bar	Maximum biocrude yield 40.8 wt%	[55]
Palm oil	Ni/HUSY catalysts	Hydrothermal conversion at 400 °C	Liquid yield 59.4%, alkane selectivity 69.4% (C9–C18)	[56]
Palm empty fruit bunch	Zeolite catalysts (HZSM-5, HUSY, HBETA)	Catalytic pyrolysis 300–500 °C	Increased aromatic hydrocarbon formation	[57]
Palm empty fruit bunch + LDPE	Clinoptilolite (natural zeolite)	Catalytic co-pyrolysis 500 °C	Bio-oil yield 72.6%, hydrocarbon content 77.6%	[58]
Palm oil	W-modified MoNiP catalyst	360 °C, 3 MPa H_2	100% conversion, isoparaffin selectivity 70.6%	[59]
Biodiesel (B100) from palm oil	WOx/SiO_2 catalyst	Hydrogen-free catalytic upgrading	Formation of SAF (C9–C14) and green diesel (C15–C18) precursors	[60]
Palm oil	CuNi LDH@Al isopropoxide catalyst	Catalytic deoxygenation	Hydrocarbon yield 77.72%, n-C17 selectivity 92.55%	[61]
Palm fatty acid distillate (PFAD)	Ni/MOF-Cr_2O_3	320 °C, 3 h	Hydrocarbon yield 93%, n-C15 + C17 selectivity 91%	[62]
Palm kernel shell + oily sludge	NiO/MMT composite catalyst	Microwave co-pyrolysis	Enhanced hydrocarbon fraction and reduced oxygenated compounds	[63]
Rapeseed oil	Sulfided Ni, Mo and NiMo catalysts	Fixed-bed reactor at 260–360 °C, 3.5–15 MPa, and 0.25–4 h	100% at 280 °C in 1 h; C17, C18 n-alkanes and i-alkanes	[64]
Rapeseed oil	Sulfided NiMo over SiO_2, Al_2O_3 and TiO_2	Fixed-bed reactor, 260–300 °C, WHSV: 2–8 h^{-1}	NiMo catalysts (3.3 wt% Ni and 15.0 wt% Mo) and used in deoxygenation of rapeseed oil in presence of hydrogen (3.5 MPa) at 260–300 °C and liquid feed weight-hourly space velocity in the range 2–8 h^{-1}.	[65]
Soybean Oil	Sulfided NiMo/γ-Al_2O_3 CoMo/γ-Al_2O_3	Batch reactor, 400 °C, 9.2 MPa, 2 h	92.9% (NiMo), 78.9% (CoMo), n-alkane: 43 wt% (CoMo), 66 wt% (NiMo)	[66]
Waste cooking oil (Dodecane as a solven)	Supported CoMoS	Fixed bed microreactor, 275 °C, 7.58 MPa, 220 h, LHSV: 3 h^{-1}	n-alkanes (C15-C18) and alkene	[67]

can promote cracking and aromatization reactions to increase the distribution of hydrocarbons towards jet fuel ranges [45]. On the other hand, thermochemical processes such as pyrolysis or hydrothermal liquefaction applied to lignocellulosic residues can produce less liquid fuel fractions; however, these technologies remain relevant because they allow the conversion of agricultural wastes. In summary, the data indicate that the best method for producing high yield SAF involves the combination of optimized catalysts with triglyceride feedstocks. On the

other hand, residues from biomass could represent alternative sources of biofuels in future integrated biorefineries [46].

The performance of the present hydrogen-free sulfide catalyst is discussed in the context of previously reported systems; however, a direct comparison must be approached with caution due to fundamental differences in reaction conditions. Most literature studies employ Ni-, Co-, or Mo-based catalysts under externally supplied H_2, whereas the current system operates under hydrogen-free conditions, relying on in situ hydrogen generation. As a result, the dominant reaction pathways, particularly the balance between hydrodeoxygenation (HDO) and direct deoxygenation (DO), differ significantly. In addition, key operational parameters such as weight hourly space velocity (WHSV), hydrogen partial pressure, feedstock composition, and reactor configuration (batch vs. continuous flow) vary widely across studies and are not consistently reported, preventing meaningful normalization. Therefore, the comparison presented here is intended to provide a qualitative perspective on catalytic behavior and mechanistic trends rather than a quantitative assessment of relative performance. Particular attention is given to how catalyst composition and acidity influence the preference for DO versus HDO pathways under differing reaction environments.

5. Conclusion

This study demonstrates that Co-Mn sulfide nanocatalysts supported on alumina provide an efficient platform for hydrogen-free DO of WCO, achieving high diesel-range hydrocarbon yields and selectivity. The exceptional performance arises from the synergistic interplay of Co_3S_4 and MnS domains, combined with interfacial Al_2S_3, which optimally tune acidity, electron density, pore accessibility, and active edge sites. The $CoS_{0.5}MnS_{0.5}$/Al composition exhibits the best balance of acid strength and density, enabling selective C—O bond cleavage while minimizing over-cracking and coke formation, and demonstrating thermal stability and resistance to deactivation. Reaction temperature, WHSV, and nitrogen flow critically influence the hydrodeoxygenation and decarboxylation pathways, highlighting the interplay between catalyst architecture and mass transport in controlling green-diesel formation. This study establishes a clear structure–property–performance relationship, providing a rational framework for designing next-generation sulfided catalysts. Overall, the Co-Mn sulfide/Al_2O_3 platform offers a scalable, robust, and sustainable approach for converting waste lipids into drop-in diesel hydrocarbons, advancing circular-economy fuel technologies.

CRediT authorship contribution statement

Laith K. Obeas: Data curation, Conceptualization. **G. Abdulkareem Alsultan:** Writing – review & editing, Writing – original draft, Supervision, Methodology. **G. Mohamed Alsultan:** Methodology, Investigation. **N. Asikin-Mijan:** Writing – review & editing, Writing – original draft, Supervision, Conceptualization. **N. Asma-Samsudin:** Writing – review & editing, Formal analysis. **Hwei Voon Lee:** Visualization, Validation, Resources. **Stella Jovita:** Validation, Funding acquisition, Formal analysis, Data curation. **Didik Prasetyoko:** Writing – review & editing, Supervision, Funding acquisition. **Maadh Fawzi Nassar:** Resources, Project administration, Investigation. **Tonni Agustiono Kurniawan:** Writing – original draft, Funding acquisition. **Dai-Viet N. Vo:** Writing – original draft, Methodology, Investigation. **Yun HinTaufiq-Yap:** Writing – original draft, Supervision.

Declaration of competing interest

There are no conflicts to declare.

Acknowledgement

This research is funded by the Indonesian Endowment Fund for Education (LPDP) on behalf of the Indonesian Ministry of Higher Education, Science, and Technology, and managed under the EQUITY Program (Contract No. 4299/B3/DT.03.08/2025 and No. 3029/PKS/ITS/2025). The research also was funded by Universiti Kebangsaan Malaysia research grant Dana Impak Perdana 2.0 (DIP 2.0) through the grant number: DIP-2024-027. Additional funding was provided by the financial support from the PUTRA Grant-UPM (Vot No: 9344200), MOSTI-e Science (Vot No: 5450746), Geran Putra Berimpak (GPB) UPM/800-3/3/1/GPB/2018/9658700 and Higher Institution Centre of Excellence (HICoE) program (JPT(BKPI)1000/016/018/28 Jld.3(2) & NANOCAT-2024E).

Appendix A. Supplementary data

Supplementary data to this article can be found online at https://doi.org/10.1016/j.fuproc.2026.108465.

Data availability

Data will be made available on request.

References

[1] M.A. Ismael, M. El-Adawy, A.S. Farooqi, M. Hamdy, M.Z. Shahid, Z. Elserfy, M. A. Nemitallah, Sustainable aviation fuel: Operational challenges, techno-economics, and life cycle analysis, Energy Fuel 39 (2025) 13848–13878.
[2] C.D. Singh, Green Energy Technologies, Digitization and Manufacturing Performance: An Environmental Perspective, 2026, pp. 1–49.
[3] W. Liu, H. Guo, D. Guo, X. Han, N. Bingwa, S.L. Rokhum, Y. Xu, B. Tang, Q. Xiao, G. Li, Microwave-absorbing CaO-CNT catalyst for enhanced transesterification: Bridging dielectric loss to energy-efficient fatty acid methyl ester production, ACS Sustain. Chem. Eng. 13 (2025) 18795–18809.
[4] S. Xia, J. Tao, G. Zhu, Z. Wang, B. Yan, W. Li, Z. Cheng, G. Chen, Comparison between thermal and electrochemical transesterification of WCO towards biodiesel production: operation parameters optimization and thermal degradation characteristics evaluation, Biomass Convers. Biorefinery (2025) 1–17.
[5] Y. Bansod, K. Ghasemzadeh, C. D'Agostino, Techno-economic assessment of biodiesel-derived crude glycerol purification processes, RSC Sustain. 3 (2025) 2605–2618.
[6] G.N. Singh, R.S. Bharj, Study of physical-chemical properties for 2nd generation ethanol-blended diesel fuel in India, Sustain. Chem. Pharm. 12 (2019) 100130.
[7] S. Kuppusamy, N.R. Maddela, M. Megharaj, K. Venkateswarlu, An overview of total petroleum hydrocarbons, in: Total Petroleum Hydrocarbons: Environmental Fate, Toxicity, and Remediation, 2019, pp. 1–27.
[8] M.N. Nabi, W.K. Hussam, M.G. Rasul, A.A. Chowdhury, M.I. Jahirul, R. Yasmin, P. Brooks, N. Islam, A.H. Marafie, Novel biofuels derivation and characterisation from *Macadamia integrifolia*, undaria pinnatifida and tree mulch via advanced pyrolysis, Int. J. Energy Res. 2025 (2025) 6049005.
[9] T. Li, S. Wang, Z. Sun, Y. Wang, J. Su, Y. Lv, L. Zhang, Z. Tao, Y. Yang, Synthesis, characterization, and application of amorphous silica–aluminas support for Fischer–Tropsch wax hydrocracking catalysts, ACS Omega 9 (2024) 36741–36750.
[10] Q. Li, D. Gunawan, L. Jiang, R. Gunawan, G. Gunasekara, S. Sarmin, R. Doyle, Q. Lai, R. Amal, J. Scott, Recent advances in electrochemical organic waste reforming: Highlights on anodic chemistry, materials design, and system integration, ACS Appl. Eng. Mater. 3 (2025) 21–43.
[11] M. Dai, Y. Qin, L. Chen, X. Chen, A review of reversible hydrogenation and dehydrogenation catalysts for liquid organic hydrogen carriers, Catal. Sci. Technol. 15 (2025) 2440–2449.
[12] Zulqarnain, S. Kim, D. Chun, J. Yoo, S.J. Yoon, S.-J. Kim, S.-J. Park, Low-temperature steam reforming of toluene as a biomass tar model compound over biochar-supported catalysts, Biochar 7 (2025) 42.
[13] C. Cheng, H. Zhao, Y. Yang, D. Shen, X. Jiang, Fe-promoted ni nanocatalysts for hydrogenolysis of klason lignin to monophenols, Biomass Bioenergy 191 (2024) 107449.
[14] A.A. Mohammed, J.H. Tannous, Catalytic hydrodeoxygenation of phenols and cresols to gasoline range biofuels, Chem. Rec. 24 (2024) e202400092.
[15] P. Huang, J. Chu, Z. Zhang, C. Zhao, Y. Guo, Optimizing alkali metal Salt-Induced structural assembly of Ni-MgO dual function materials for enhanced CO2 capture and methanation performance, Chem. Eng. Sci. 294 (2024) 120120.
[16] L. Zhang, Y. Gao, X. Bai, L. He, W. Fu, T. Tang, Ni catalyst on ZSM-22 nanofibers bundles with good catalytic performance in the hydroisomerization of n-dodecane, Fuel 357 (2024) 129885.
[17] E. Ramos-Fernández, V.K. Velisoju, J. Gascon, P. Castaño, Engineering Metal-MOF interfaces for selective CO_2 hydrogenation to methanol, Chem. Eur. J. 31 (2025) e202403709.
[18] B. Li, A. Ali, S. Lei, C. Zhao, Lipids to fuels and chemicals, in: Heterogeneous Catalysis for Sustainable Energy, 2022, pp. 459–506.

[19] C. Zhao, J. Luo, W. Zhu, Y. Li, C. Liang, Efficient hydrodeoxygenation of methyl palmitate over NiMo/ZrO2 catalyst with electron transfer between Ni and Mo, Catal. Today 437 (2024) 114780.
[20] S.D. Foraita, Investigation of Ni/ZrO 2 Catalysts for the Hydrodeoxygenation of Microalgae Oil, Technische Universität München, 2017.
[21] H. Deng, F. Luo, G. Feng, R. Zhang, R. Ye, Research progress and prospects of ZrO2-based catalysts in CO2 hydrogenation, Carbon Hydrogen 27 (2025) 401–419.
[22] A. Samikannu, M. Mani, L.J. Konwar, P. Mäki-Arvela, P. Virtanen, J.-P. Mikkola, Hydrodeoxygenation of Triglycerides into Renewable Diesel, 2025.
[23] H. Du, Z. Shao, A review on modulating oxygen vacancy defect of catalysts to promote CO2 reduction reaction to CO, Energy Fuel 39 (2025) 5672–5690.
[24] V. Yakovlev, S. Khromova, O. Sherstyuk, V. Dundich, D.Y. Ermakov, V. Novopashina, M.Y. Lebedev, O. Bulavchenko, V. Parmon, Development of new catalytic systems for upgraded bio-fuels production from bio-crude-oil and biodiesel, Catal. Today 144 (2009) 362–366.
[25] S. Thongkumkoon, W. Kiatkittipong, U.W. Hartley, N. Laosiripojana, P. Daorattanachai, Catalytic activity of trimetallic sulfided Re-Ni-Mo/γ-Al2O3 toward deoxygenation of palm feedstocks, Renew. Energy 140 (2019) 111–123.
[26] A. Srifa, K. Faungnawakij, V. Itthibenchapong, S. Assabumrungrat, Roles of monometallic catalysts in hydrodeoxygenation of palm oil to green diesel, Chem. Eng. J. 278 (2015) 249–258.
[27] T. Burimsitthigul, B. Yoosuk, C. Ngamcharussrivichai, P. Prasassarakich, Hydrocarbon biofuel from hydrotreating of palm oil over unsupported Ni–Mo sulfide catalysts, Renew. Energy 163 (2021) 1648–1659.
[28] A. Afiqah-Idrus, G. Abdulkareem-Alsultan, N. Asikin-Mijan, M.F. Nassar, L. Voon, S.H. Teo, T.A. Kurniawan, N.A. Adzahar, M. Surahim, S.Z. Razali, Deoxygenation of waste sludge palm oil into hydrocarbon rich fuel over carbon-supported bimetallic tungsten-lanthanum catalyst, Energy Convers. Manage.: X 23 (2024) 100589.
[29] G. Abdulkareem-Alsultan, N. Asikin-Mijan, L.K. Obeas, R. Yunus, S.Z. Razali, A. Islam, Y.H. Taufiq-Yap, In-situ operando and ex-situ study on light hydrocarbon-like-diesel and catalyst deactivation kinetic and mechanism study during deoxygenation of sludge oil, Chem. Eng. J. 429 (2022) 132206.
[30] S.Z. Razali, R. Yunus, D. Kania, S.A. Rashid, L.H. Ngee, G. Abdulkareem-Alsultan, B.M. Jan, Effects of morphology and graphitization of carbon nanomaterials on the rheology, emulsion stability, and filtration control ability of drilling fluids, J. Mater. Res. Technol. 21 (2022) 2891–2905.
[31] H. Chang, G. Abdulkareem-Alsultan, Y. Taufiq-Yap, S.M. Izham, S. Sivasangar, Development of porous MIL-101 derived catalyst application for green diesel production, Fuel 355 (2024) 129459.
[32] T.A. Kurniawan, M. Ali, A. Mohyuddin, A. Haider, M.H.D. Othman, A. Anouzla, H. H. Goh, D. Zhang, W. Dai, F. Aziz, Innovative transformation of palm oil biomass waste into sustainable biofuel: technological breakthroughs and future prospects, Process. Saf. Environ. Prot. 193 (2024) 643–664..
[33] K.C. Goh, T.A. Kurniawan, G.A. AlSultan, M.H.D. Othman, A. Anouzla, F. Aziz, I. Ali, J.C.C. Casila, M.I. Khan, D. Zhang, Innovative circular bioeconomy and decarbonization approaches in palm oil waste management: a review, Process Saf. Environ. Prot. 195 (2025) 106746.
[34] F. Alshaeer, M. Zorah, H.M. Mahmoud, L. Abdalgadir, A.G. Taki, B.A. Mohammed, G. Abdulkareem-Alsultan, M.F. Nassar, Bandgap-engineered MXene-g-C3N4 interfacial layer for enhanced charge carrier dynamics in perovskite solar cells, J. Alloys Compd. 1011 (2025) 178247.
[35] A.A. Dabbawala, W. Al Maksoud, E. Abou-Hamad, N.D. Charisiou, A. Constantinou, E. Harkou, A.I. Latsiou, S. AlKhoori, S.J. Hinder, M.A. Baker, D.H. Anjum, Y. Kobayashi, M.A. Goula, K. Polychronopoulou, Tuning of the acid sites in the zeolite-alumina composite Ni catalysts and their impact on the palm oil hydrodeoxygenation reaction, Chem. Eng. J. 493 (2024).
[36] S. Alkhoori, S. Alareeqi, A.A. Dabbawala, G. Siakavelas, A. Latsiou, D.H. Anjum, M. Harfouche, M.A. Vasiliades, S.J. Hinder, M.A. Baker, M. Khaleel, D. Bahamon, L. F. Vega, M.A. Goula, A.M. Efstathiou, K. Polychronopoulou, Steering palm oil hydrodeoxygenation towards biofuel production: an experimental and theoretical approach to unveil periodic trends, Mater. Today Chem. 40 (2024).
[37] K.A. Samawi, B.A. Mohammed, E.A.-A. Salman, H.M. Mahmoud, A.Z. Sameen, S. M. Mohealdeen, G. Abdulkareem-Alsultan, M.F. Nassar, Vertical growth of a 3D Ni–Co-LDH/N-doped graphene aerogel: a cost-effective and high-performance sulfur host for Li–S batteries, Phys. Chem. Chem. Phys. 26 (2024) 9284–9294.
[38] N. Mansir, H.M. Sidek, S.H. Teo, N.-A. Mijan, A.G. Alsultan, C.H. Ng, M. R. Shamsuddin, Y.H. Taufiq-Yap, Catalytically active metal oxides studies for the conversion technology of carboxylic acids and bioresource based fatty acids to ketones: a review, Bioresour. Technol. Rep. 17 (2022) 100988.
[39] F. Batool, T.A. Kurniawan, A. Mohyuddin, M.H.D. Othman, I. Ali, G. AbdulKareem-Alsultan, A. Anouzla, H.H. Goh, D. Zhang, F. Aziz, Rosa damascena waste as biosorbent for co-existing pollutants removal: Fixed-bed column study and ANN modeling, Chem. Eng. Sci. 293 (2024) 120057.
[40] K.A. Samawi, E.A.-A. Salman, B.A.-A. Alshekhly, M.F. Nassar, M.Y. Borzehandani, G. Abdulkareem-Alsultan, M.A.M. Latif, E. Abdulmalek, Rational design of different π-bridges and their theoretical impact on Indolo [3, 2, 1-jk] carbazole based dye-sensitized solar cells, Comp. Theoret. Chem. 1212 (2022) 113725.
[41] S.H.H. Al-Jaberi, U. Rashid, F.A.J. Al-Doghachi, G. Abdulkareem-Alsultan, Y. H. Taufiq-Yap, Synthesis of MnO-NiO-SO_4^{2}/ZrO_2 solid acid catalyst for methyl ester production from palm fatty acid distillate, Energy Convers. Manag. 139 (2017) 166–174.
[42] A.-A. G, A. Islam, J. Janaun, M.S. Mastuli, Y.H. Taufiq-Yap, Synthesis of structured carbon nanorods for efficient hydrogen storage, Mater. Lett. 179 (2016) 57–60.
[43] F.H. Kamil, A. Salmiaton, R.M.H.R. Shahruzzaman, R. Omar, A.G. Alsultsan, Characterization and application of aluminum dross as catalyst in pyrolysis of waste cooking oil, Bull. Chem. React. Eng. Catalys. 12 (2017) 81–88.
[44] K.A. Samawi, S.J. Abdulrazzaq, M. Zorah, M. Al-Bahrani, H.M. Mahmoud, G. Abdulkareem-Alsultan, A.G. Taki, M.F. Nassar, MoS_2/graphdiyne nanotube/MXene 3D-interconnected ternary aerogel: a high-performance electrocatalyst for hydrogen evolution reaction, J. Solid State Chem. 334 (2024) 124690.
[45] N.A. Adzahar, G. AbdulKareem-Alsultan, N.A. Mijan, M. Mastuli, H. Lee, Y. Taufiq-Yap, Effect of catalyst synthesis of bimetallic nickel-cobalt supported iron-based catalysts on converting palm kernel oil into bio-jet fuel via deoxygenation reaction, Energy 314 (2025) 133957.
[46] L.N.S. Freitas, N.P. Lopes, F.P. de Sousa, V.M. Pasa, Catalytic pyrolysis of macauba oils over eggshell-derived and commercial CaO for sustainable biohydrocarbon production to biogasoline, SAF, and green diesel formulation, J. Anal. Appl. Pyrolysis 194 (2026) 107546.
[47] A. Nugroho, P.D.C. Dewi, L.N. Hidayati, A. Kristiani, F. Aulia, A.N. Bakti, J. Prasetyo, N. Rinaldi, D. Dahnum, Catalytic deoxygenation of coconut oil to bio-jet fuel range hydrocarbon over nickel on ZIF-67-derived metal oxide, Fuel 407 (2026) 137430.
[48] N.A. Adzahar, G. AbdulKareem-Alsultan, N.A. Mijan, M. Mastuli, H. Lee, Y. Taufiq-Yap, Enhancing aviation sustainability: Bimetallic Ni–Co catalysts for bio-jet fuel from palm kernel oil, Fuel 405 (2026) 136388.
[49] F.P. de Sousa, V.M. Pasa, Catalytic deoxygenation of palm oils to produce bio-hydrocarbons in the range of sustainable aviation fuels (SAF) and green diesel over Nb2O5, Mol. Catal. 585 (2025) 115354.
[50] J. Ahmad, A. Chotirattanachote, S. Sedtabute, U. Rashid, C. Ngamcharussrivichai, Hydrogen-free catalytic hydrothermolysis of palm oil into sustainable aviation fuel-range hydrocarbons over Ni/AC–Al2O3 catalysts, Process. Saf. Environ. Prot. 204 (2025) 108139.
[51] N. Valentino, O. Farobie, D.A. Sugeng, H.N. Anindita, I. Masfuri, N. Rahmawati, T. P. Rini, T. Anggoro, A. Syafrinaldy, E. Rosyadi, Enhancing bio-oil quality and hydrogen recovery through co-pyrolysis of empty fruit bunch and polypropylene over a NiFe/ZSM-5 catalyst, Biomass Bioenergy 206 (2026) 108652.
[52] N. Unsomsri, N. Unsomsri, S. Kaewluan, S. Tawkaew, S. Wiriyasart, Enhancing bio-oil yield and quality from palm kernel shells via co-pyrolysis with palm fresh fruit in a double auger reactor, J. Anal. Appl. Pyrolysis 195 (2026) 107632.
[53] N. Unsomsri, S. Wiriyasart, S. Tawkaew, S. Kaewluan, Influence of pyrolysis temperature on crude palm pyrolysis oil from fresh palm fruit bunches in a double-inclined screw reactor, J. Anal. Appl. Pyrolysis 192 (2025) 107250.
[54] N. Hongloi, T. Rahman, F. Feyzbar-Khalkhali-Nejad, C. Prapainainar, P. Wongsurakul, E. Aransiola, L. Zhang, P. Bargiela, J. Baltrusaitis, P. Prapainainar, Palm oil deoxygenation with glycerol as a hydrogen donor for renewable fuel production using nickel-molybdenum catalysts: the effect of support, Fuel Process. Technol. 270 (2025) 108196.
[55] R.H. Teoh, L.Y. Lee, S. Gan, H.K. Ng, S. Thangalazhy-Gopakumar, Production of biocrude oil through hydrothermal liquefaction of palm empty fruit bunch with ethanol co-solvent: a source of value-added chemicals, Chem. Eng. Res. Des. 218 (2025) 455–467.
[56] S. Sedtabute, T. Vitidsant, C. Ngamcharussrivichai, Structure–acidity interplay in Ni/HUSY catalysts for external h2-free hydrothermal conversion of palm oil in alcohol–water media, Biomass Bioenergy 211 (2026) 109152.
[57] A. Chotirattanachote, J. Ratthiwal, C. Samart, U. Rashid, N. Hinchiranan, C. Ngamcharussrivichai, J. Ahmad, Unlocking high-value bio-chemicals: Pyrolysis-GC/MS study of thermal and zeolite-catalyzed decomposition of local palm oil empty fruit bunches (PEFB), Biomass Bioenergy 206 (2026) 108598.
[58] M.A. Al-Maari, M.A. Ahmad, A.T.M. Din, H. Hassan, A.M. Alsobaai, Upgrading bio-oil production via catalytic co-pyrolysis of oil palm empty fruit bunch and low-density polyethylene using clinoptilolite catalyst, J. Anal. Appl. Pyrolysis 186 (2025) 106937.
[59] C. Yin, X. Li, Z. Li, Y. Han, Y. Guo, Z. Ma, X. Li, D. Liu, H. Zhao, B. Liu, W-modified unsupported MoNiP catalysts synergistically enhancing palm oil hydrodeoxygenation-isomerization to low-freezing-point biofuels, Fuel 409 (2026) 137865.
[60] M. Solehudin, K. Wengwirat, P. Promchana, Y. Poo-arporn, W. Limphirat, K. Choojun, T. Sooknoi, Bifunctional WOx/SiO2 catalysts for hydrogen-free upgrading of b100 and bio-ethylene to SAF and green diesel precursors via olefin metathesis and deoxygenation, Fuel 420 (2026) 138769.
[61] N.A. Ibrahim, T.A.-A. Jwaid, L.K. Obeas, G. Abdulkareem-Alsultan, N. Asikin-Mijan, S. Samidin, N. Asma-Samsudin, M.F. Nassar, H. Lee, Y.H. Taufiq-Yap, Mechanistic insights into green diesel production via CuNi LDH@ Al isopropoxide-catalyzed palm oil deoxygenation: a study using in-situ XAS and DFT, FlatChem 55 (2025) 100973.
[62] H. Chang, H.V. Lee, Y.H. Taufiq-Yap, G. Abdulkareem-Alsultan, S. Seenivasagam, Metal organic framework-derived advanced porous material supported catalysts for green diesel production from palm fatty acid distillate via deoxygenation pathways, Renew. Energy 238 (2025) 121882.
[63] D. Chu, W. Su, W. Zhang, Z. Cao, Microwave catalytic co-pyrolysis of palm kernel shell and oily sludge: synergistic effects and bio-oil analysis, J. Anal. Appl. Pyrolysis 196 (2026) 107712.
[64] P. Šimáček, D. Kubička, G. Šebor, M. Pospíšil, Fuel properties of hydroprocessed rapeseed oil, Fuel 89 (2010) 611–615.

[65] D. Kubička, J. Horáček, M. Setnička, R. Bulánek, A. Zukal, I. Kubičková, Effect of support-active phase interactions on the catalyst activity and selectivity in deoxygenation of triglycerides, Appl. Catal. B Environ. 145 (2014) 101–107.
[66] B. Veriansyah, J.Y. Han, S.K. Kim, S.-A. Hong, Y.J. Kim, J.S. Lim, Y.-W. Shu, S.-G. Oh, J. Kim, Production of renewable diesel by hydroprocessing of soybean oil: effect of catalysts, Fuel 94 (2012) 578–585.
[67] H. Wang, G. Li, K. Rogers, H. Lin, Y. Zheng, S. Ng, Hydrotreating of waste cooking oil over supported CoMoS catalyst–catalyst deactivation mechanism study, Mol. Catal. 443 (2017) 228–240.